Magmatic fractionation and the magmatic-hydrothermal transition in rare metal granites: evidence from argemela (central portugal)

Julie Anne-Sophie Michaud, Michel Pichavant

Journal Pre-proofs

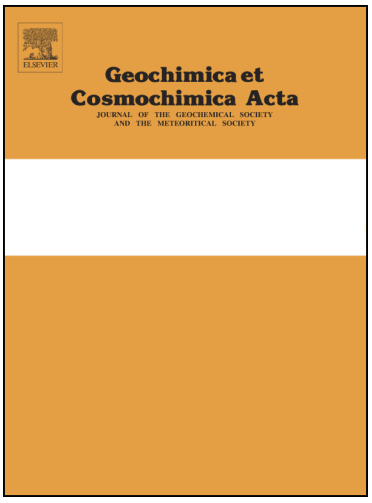

Magmatic fractionation and the magmatic-hydrothermal transition in rare metal granites: evidence from argemela (central portugal)

Julie Anne-Sophie Michaud, Michel Pichavant

PII: S0016-7037(20)30539-1
DOI: https://doi.org/10.1016/j.gca.2020.08.022
Reference: GCA 11894

To appear in: *Geochimica et Cosmochimica Acta*

Received Date: 23 October 2019
Revised Date: 19 August 2020
Accepted Date: 20 August 2020

Please cite this article as: Anne-Sophie Michaud, J., Pichavant, M., Magmatic fractionation and the magmatic-hydrothermal transition in rare metal granites: evidence from argemela (central portugal), *Geochimica et Cosmochimica Acta* (2020), doi: https://doi.org/10.1016/j.gca.2020.08.022

MAGMATIC FRACTIONATION AND THE MAGMATIC-HYDROTHERMAL TRANSITION IN RARE METAL GRANITES: EVIDENCE FROM ARGEMELA (CENTRAL PORTUGAL)

Julie, Anne-Sophie Michaud[1*] and Michel Pichavant[1]

[1] Université d'Orléans/CNRS/ISTO/BRGM, UMR 7327, 1A rue de la Férollerie, 45071 Orléans, France

[*] julie.michaud@outlook.fr

ABSTRACT

Rare Metal Granites (RMGs) are highly evolved intrusions with specific geochemical signatures that are the result of combined magmatic and hydrothermal processes. In most examples, the early evolution is overprinted by late subsolidus transformations and the role of magmatic and magmatic-hydrothermal fractionation processes remains unclear. The origin of fluids involved in magmatic-hydrothermal systems is also an open question. The Argemela RMG (Portugal) is a small subvolcanic intrusion, which exposes in remarkable continuity a sequence of magmatic, magmatic-hydrothermal and early hydrothermal processes. The intrusion comprises a main granitic facies and a border unit made of a complex alternation of aplitic and pegmatitic facies plus three generations of intragranitic veins. The granitic mineral assemblage includes quartz, K-feldspar, albite, muscovite and accessory montebrasite, cassiterite and columbite-tantalite. The whole-rock chemistry is strongly peraluminous, with very high P_2O_5, Li and F enrichments, elevated rare metal (Sn, Nb, Ta, W) concentrations and strong depletions in Ca, Fe, Ti, Mg. Trace element zonation in minerals, mainly muscovite and quartz, record crystallization/fractionation processes along the magmatic-hydrothermal transition. Three main stages are recognized, magmatic (crystal fractionation and accessory/minor mineral saturation), magmatic-hydrothermal (fluid/melt element partitioning) and early hydrothermal, corresponding to the segregation and collection of magmatic fluids in the intragranitic vein system. Those are followed by limited metasomatic transformations and a late sulphide stage. Stable isotope (O, H) data demonstrate a magmatic origin

for the early fluids and a granite-buffered signature for the vein-forming fluids. The fractionation of rare elements (Sn, Nb, Ta, Li, W, Mn, B, Rb, Cs) from the magmatic to the early hydrothermal stage is quantitatively modelled from the combination of three mechanisms, crystal fractionation, magmatic crystallization of accessory/minor phase (MCMA) and fluid/melt partitioning. Sn and W show a markedly contrasted behaviour with Sn precipitated as disseminated mineralization within the intrusion and W partitioned toward the magmatic fluid and extracted from the intrusion. Geochemical trends along the magmatic-hydrothermal transition do not require phases with unusual properties, such as immiscible hydrous melts to be explained and they do not necessarily result in an amplification of initial rare metal melt enrichments. The Argemela RMG stresses the importance of MCMA to generate magmatic rare element pre-concentrations, which later can be hydrothermally redistributed to form large economic deposits.

Keywords: rare element fractionation, magmatic-hydrothermal transition, granite, stable isotopes, fluids

1. INTRODUCTION

Rare Metal Granites (RMGs), also designated as tin, topaz, zinnwaldite or Li-F granites, are highly evolved granites, characterized by a specific geochemical signature - i.e., elevated concentrations in fluxing elements (F, B, P, Li), significant depletions in REE, Y, Ca, Fe, Ba and Sr and marked enrichments in rare lithophile elements and metals (Sn, Nb, Ta, Be, Cs, Rb and W; see Černý et al., 2005; Linnen and Cuney, 2005) - which strongly differs from most other granites. RMGs occur worldwide, such as in China (Belkasmi et al., 2000), Finland (Haapala and Likkari, 2005), Nigeria (Kinnaird et al., 1985), Egypt (Zoheir et al., 2020), Canada (Kontak, 1990), Russia (Raimbault et al., 1995) and Western Europe (Charoy and Noronha, 1996; Breiter et al., 2017; Manning and Hill, 1990). The source of rare elements in peraluminous RMGs and the origin of their geochemical specificities have been strongly controversial topics since the 1960's. There is now general agreement that both magmatic (melt-driven) and hydrothermal (fluid-driven) processes are involved in the genesis of RMGs (Beus et al., 1962; Beus and Zhalashkova, 1964; Zhalashkova and Sitnin, 1967; Kovalenko, 1976; Hu et al., 1984; Pichavant et al. 1988a, b; Raimbault and Burnol, 1998). However, evaluating the respective importance of each group of processes continues to be an area of active research.

In most natural RMGs, the early evolution is obliterated by late subsolidus metasomatic processes, such as greisenization (e.g., Pollard et al. 1987; Štemprok, 1987; Breiter et al., 2017) and kaolinization (Fouillac and Rossi, 1991; Cuney et al., 1992; Raimbault et al., 1995). Consequently, the roles of magmatic (partial melting, mineral saturation and fractionation) and magmatic-hydrothermal (fluid/melt partitioning) processes on RMGs geochemical signatures are still unclear. Several models of the magmatic-hydrothermal transition (MHT, defined here as the transition from a melt-driven to a fluid-driven crystallization/fractionation regime) have been proposed recently from studies of rare element pegmatites (Kontak and Kyser, 2009; Hulsbosch et al., 2014; Kaeter et al., 2018; Hulsbosch, 2019). Immiscible hydrous melts are postulated (e.g., Thomas and Davidson, 2012; 2016) and fractionation assumed to follow element partitioning between three phases, silicic melt, aqueous melt and hydrothermal fluid (e.g., Kaeter et al., 2018). However, the concept of immiscible hydrous melts has so far not received confirmation (London, 2015; Thomas and Davidson, 2016), which stresses the need for alternative fractionation models in rare metal magmas. Another critical issue in magmatic-hydrothermal systems concerns the origin of fluids. Crystallization of anhydrous magmatic phases builds up the H_2O concentration in the residual melt (e.g., Jahns and Burnham, 1969), ultimately leading to the exsolution of a magmatic fluid (e.g., Smith et al., 1996; Harlaux et al., 2018; Korges et al., 2018). However, some magmas of crustal origin are fluid-saturated very early on during their evolution (e.g., Le Fort et al., 1987). Non-magmatic (metamorphic and/or meteoric) fluids can be present in and around granitic plutons (Kelly and Rye, 1979; Fouillac and Rossi, 1991; Polya et al., 2000). In some systems, hydrothermal fluids from various sources can superimpose (e.g., Sheppard, 1977; Vallance et al., 2001).

This paper presents geochemical data (major and trace element data on whole-rocks and minerals, O and H stable isotope data) on the Argemela rare metal granite (Central Portugal), a small subvolcanic intrusion in the Portuguese part of the Central Iberian Zone (Charoy and Noronha, 1996; Michaud, 2019). The intrusion is mostly free of subsolidus processes, such as greisenization and kaolinization and it allows the early stages of fractionation to be documented. A sequence of magmatic, magmatic-hydrothermal and early hydrothermal processes is exposed in remarkable continuity for a small intrusion. Petrographical, mineralogical and textural studies allow the successive stages of RMG crystallization along the MHT to be described. Three main fractionation mechanisms are identified from the quantitative modelling of trace element zonation in muscovite, using mineral/melt, fluid/melt partition coefficients and accessory mineral solubility data. The magmatic origin

of early and vein-forming hydrothermal fluids is demonstrated from the stable isotope data. Results are incorporated in a model of magmatic and magmatic-hydrothermal evolution and implications for fractionation mechanisms and element transport and deposition in rare metal magmas are discussed.

2. GEOLOGICAL SETTING

The Argemela granite (Fig. 1) is located in the southern part of the Central Iberian Zone (CIZ), mainly made of autochthonous Gondwanan terranes corresponding to low grade external metamorphic zones. Occurring ~13 km east of the world class Panasqueira W mine and ~1.5 km west of the Fundão composite granite, the Argemela granite forms a small almost elliptical body (i.e., 250 x 125 m) in map view and is characterized by a pipe-like geometry in cross-section extending to a maximum depth of 1 km (Michaud, 2019). Contacts of the granite with the surrounding low-grade Beira schists (Schist and Greywacke Complex (SGC) of Neo-Proterozoic to Cambrian age) are mostly intrusive except for the northeastern contact, which is affected by a dextral shear corridor (Michaud, 2019).

The Argemela stock was exploited by Felmica Minerais Industriais SA as a source of ceramic raw materials, and the quarry (on the northeastern part) provides a well exposed view of the granite. The Argemela intrusion is composed of two main units: (i) the *granitic* unit (Fig. 1, 2a), which forms the most part of the granite and (ii) the *border* unit (Fig. 1a, b, 2b, c). The granitic facies, already described in Charoy and Noronha (1996), is characterized by a subvolcanic texture. Millimetric phenocrysts of "snowball" euhedral quartz and silverish to greenish micas are embedded in a fined-grained white matrix. The border unit, occurring discontinuously along the contact and mainly found in the quarry, consists in an alternation of different units (Fig. 1b). In hand samples, aplitic zones are characterized by a very fine-grained white matrix without apparent phenocrysts. These are homogeneous, particularly at the contact with the surrounding Beira Schists, to banded in more internal parts (Fig. 1b). Pegmatitic zones consist of large phenocrysts of K-feldspar embedded in a micaceous matrix. In the internal part of the border facies, large K-feldspar crystals form unidirectional solidification textures (UST) directed toward the centre of the granite (Fig. 1). The micaceous facies occurs mainly at the contact with the granitic unit and is characterized by the presence of numerous silverish to greenish

micas phenocrysts (Fig. 1b; 2c). A "ball like" facies has been described as an ovoidal mass consisting of very fine-grained material without any apparent phenocrysts and in sharp contact with the granitic facies (Charoy and Noronha, 1996). Subvertical "dyke-like" units have also been observed showing sharp contacts with the granitic facies (Fig. 2d). These units are scarce, discontinuous (i.e., pinched termination) and range from few cm to 10 cm. All units, the *granitic*, the *border* and the *"dyke-like"*, are intersected by a network of *intragranitic veins* clearly observable in the quarry (Fig. 1). Geometrical relations, structural and mineralogical data enable three generations of veins to be distinguished (see details in Michaud et al., 2020). The first and earliest generation (Type I, Fig. 2e) is characterized by an alternation of quartz, K-feldspars and montebrasite. Type II veins, which crosscut Type I veins, are K-feldspar-free, being mainly composed of quartz and scarce montebrasite. Type III veins (e.g., Fig. 2f) intersect the two previous generations and are mineralogically quite variable. One particular vein (the Santa Rita vein, SR; Fig. 1), located on the southeastern part of the granite at the contact with the country rocks, has been hand exploited for tungsten and is described in Inverno (1998). On the sheared northeastern border of the granite, sulphides occur either as disseminated in the granite, in and around intragranitic veins or in small fractures crosscutting intragranitic veins (Fig. 2g).

3. METHODS AND ANALYTICAL TECHNIQUES

3.1. Strategy and sampling

In this study, whole-rock data on representative samples of the Argemela granite and veins are combined with textural and chemical analyses (electron microprobe, LA ICP-MS) of mineral phases and stable isotope (O, H) data. Focus is placed on the characterization of in particular micas and quartz but also of K-feldspar and Li-phosphate phases, which serve as monitors of fractionation processes along the MHT.

Representative rock samples were collected from in-situ outcrops, including samples of the granitic facies, the border unit and of the three generations of veins. Observation and sampling were conducted in the quarry, in the northeastern part of the intrusion, considered as representative of the whole intrusion. Samples were prepared to produce 30 and 100 µm thick thin sections, the thickest sections being prepared specifically

for LA-ICP-MS analyses. An optical microscope was used for the initial mineralogical and textural observations.

3.2. Bulk rock analyses

Bulk rock analyses were carried out at the SARM (CRPG, Nancy, France; details are summarized in Carignan et al., 2001). Samples were analysed using an inductively coupled plasma emission spectrometer (ICP-OES) iCap6500 ThermoFisher for major elements and an inductively coupled plasma mass spectrometry (ICP-MS) iCapQ ThermoFisher for trace elements. Detection limits, calculated as the average plus 6 times the absolute standard deviation on 100 measurements of blank, are indicated in Table A.2. Samples analysed include the granitic facies and the border facies. Veins (i.e., core of the veins) and granite at vein margins were also analysed to track potential chemical variations.

3.3. SEM and cathodoluminescence imaging

Backscattered electron (BSE) images were obtained at the Institut des Sciences de la Terre d'Orléans (ISTO, France) using a Merlin compact ZEISS Microscope equipped with a Bruker EDS detector and working under an acceleration voltage of 15 kV. Cathodoluminescence images were obtained at BRGM, Orléans (France) using a MIRA TESCAN (FEG) Microscope equipped with a panchromatic (350-660 mm) cathodoluminescence (CL) detector and working with an acceleration voltage of 20-25kV.

3.4. EMPA analyses

Punctual analyses, traverses and elements distribution maps for major and minor elements were obtained using a CAMECA SX Five microprobe (Institut des Sciences de la Terre d'Orléans, France) operated under an acceleration voltage and a beam current of 15 kV and 6 nA respectively. Standards included albite (Si$K\alpha$ and Na$K\alpha$), synthetic $MnTiO_3$ (Mn$K\alpha$ and Ti$K\alpha$), Al_2O (Al$K\alpha$), Fe_2O_3 (Fe$K\alpha$), MgO (Mg$K\alpha$), andradite

(Ca*Kα*), orthoclase (K*Kα*), apatite (P*Kα*) and topaz (F*Kα*). Averages and standard deviations calculated for multiple analyses are given in the analytical tables (Annex).

3.5. LA-ICP-MS analyses

Trace element compositions of micas, quartz, Li-phosphates, and K-feldspars were analysed in different laboratories, using different instruments and conditions, summarized in Table A.1. For micas, Li-phosphates, and K-feldspars, data were standardized against Al_2O_3 (wt%), determined by electron microprobe and, for quartz, against Si (Table A.1). Standards were analysed two times at the beginning and at the end of each run and one time every 10 to 20 analyses. Raw data were processed off-line using Glitter software where time-resolved signals were examined one-by-one. When the signal was anomalous (e.g., inclusions or irregular spectra), the analysis was not considered. Element concentrations were calculated for the initial ~30 s of all ablation signals relative to the gas blank (~20 s), with a linear interpolation across standard analyses. Final concentrations were calculated based on the NIST concentrations values given by Pearce et al. (1997). For homogeneous crystals, mean values and standard deviations are calculated on the *n* analyses. For single analysis, the 1 sigma error is given in parenthesis under each value in the analytical tables (Annex).

3.6. Stable isotopes

Granite and vein samples were first crushed to obtain a coarse residue and then passed three times in a sorting machine to obtain a representative sampling. For each sorted representative sample, quartz and micas were separated by hand picking under a binocular loupe. The O and H isotopic compositions were determined at CRPG (Nancy, France) using different procedures.

O isotopes. Oxygen in quartz and micas was extracted by fluorination using BrF_5 in a high-vacuum apparatus similar to those described by Baertschi and Silverman (1951; see also Clayton, 1955; Taylor and Epstein, 1962; Clayton and Mayeda, 1963). Ten mg of each sample was loaded into pure nickel reaction tubes and outgassed under vacuum at room temperature (~30°C) for 1h before reaction with BrF_5 at 550°C for 7 to

10h. Liberated O_2 is then passed through a hot graphite rod for conversion into CO_2. $^{18}O/^{16}O$ isotopes of granite and vein samples were measured using a Thermo-Fisher MAT253 mass spectrometer and values are given as $\delta^{18}O$ in permil relative to Vienna Standard Mean Ocean Water (VSMOW). Analytical precision was quantified at ± 0.1‰ using in-house standard.

H isotopes. The D/H isotopic composition of muscovite was measured using an Elemental Analyzer (EA) coupled to a VG Isoprime Isotope Ratio Mass Spectrometer (IRMS). Micas powders were dehydrated for 48h, weighted and packed in tin capsules. Tin capsules were then loaded into an automatic sampler carousel pre-flushed with He to avoid atmospheric moisture. Samples were combusted on an EA reaction tube to reduce hydroxyls to H_2. A high temperature of 1450°C (Khantal-Superthal heating element) is necessary for a quick sample reduction avoiding formation of CH compounds. Produced gases were separated on a chromatographic column kept at 60°C prior to introduction of H_2 in the MS source and analyses of D/H. Three different internal standards (muscovite: Mus-D65, phlogopite: Mica-Mg and a fine-grained marine sediment from the Bay of Bengal: SO188) were used to estimate the instrumental drift. D/H is given as δD and normalized against SMOW. In addition, fluids trapped in quartz from the different facies were extracted and their D/H isotopic composition determined using the same method. To optimize the accuracy of the isotopic measurements, two in-house standards were weakly extracted and analysed. Samples were systematically duplicated.

4. PETROGRAPHICAL RESULTS

4.1. Granitic facies and border unit

The main petrographical, mineralogical and textural features of these two units are summarized in Table 1. The granitic facies is made of quartz and micas phenocrysts embedded in a fine-grained matrix composed mainly of albite and scarce K-feldspars. This mineralogical assemblage forms the skeleton of the granite and accessory minerals include montebrasite, cassiterite and columbite-tantalite. In the border unit, the mineralogical assemblage varies with the specific zone and the related texture.

In the granitic facies (Fig. 2a), two generations of quartz have been recognized (Qtz_I and Qtz_{II}). Quartz phenocrysts, also called snowball quartz (Qtz_I), occur as euhedral crystals up to several mm large (Fig. 3a).

Euhedral albite laths (Ab_I), from several µm to 300 µm in size, form inclusions in Qtz_I where they underline the bipyramidal habit of the host crystal. Inclusions in the inner part of Qtz_I (Ab_{Ia}) are generally less numerous but larger than in the most external part (Ab_{Ib}, Fig. 3a). SEM and cathodoluminescence imaging reveal growth zonation in snowball quartz marked by alternating light and dark zones underlined by albite laths (Qtz_{Ia}, Fig. 3a). The external part (Qtz_{Ib}) forming light grey growth zones and separated from the inner part by numerous tiny albite inclusions, is mainly anhedral and resemble "groundmass quartz" defined in Müller et al. (2009). A second type of quartz (Qtz_{II}) occurs within the matrix as polygonal grains never exceeding 100 µm. These grains can form a mosaic in "pockets" replacing early snowball Qtz_I. The same observations are made in the border units although crystal size and occurrence vary with lithological characteristics (e.g., small crystals in aplitic units). In addition, a third generation of quartz was encountered dominantly in the micaceous facies. These Qtz_{III} occur as interstitial grains within the matrix or as interstitial overgrowths on Qtz_I overprinting its original texture and zonation (Fig. 3b).

Silverish white micas occur as phenocrysts of several hundred µm to several mm, appearing either as isolated crystals or in clusters. BSE imaging reveals a quite complex chemical zonation. Several zones corresponding to at least three crystallization steps (I, II, III) can be recognized from core to rim (Fig. 3c). The internal part (Ms_I) is characterized by a light grey core (Ms_{Ia}) evolving to a brighter rim (Ms_{Ib}). Similarly, the intermediate zone (Ms_{II}), which is darker than Ms_I, comprises a core (Ms_{IIa}) and a bright rim (Ms_{IIb}). In contrast with the two first generations, Ms_{III} forms dark patchy anhedral/interstitial overgrowths or aggregates of thin laths within the matrix. This rather complex zonation is not always equally marked in all crystals - especially for Ms_{Ib} and Ms_{IIb} - and it differs from that described by Charoy et al. (1995). An additional generation of micas has been identified in the border unit (Fig. 3d) and to a lesser extent in the granitic facies in contact with the border unit. Ms_{IV} occur either as bright rims invading $Ms_{I\text{-}II\text{-}III}$ or as patchy bright zones within $Ms_{I\text{-}II\text{-}III}$. Ms_{IVa} (granitic facies) can be distinguished from Ms_{IVb} (border unit), the latter being brighter than the former in BSE imaging.

Albites occur either as inclusions in snowball quartz (see above; Fig 3a) and as the main minerals of the matrix (Ab_{II}; Fig. 3e). They range from tens to 500 µm in the matrix, are mostly euhedral and show the typical albite twinning. In most units, K-feldspars (Kfs_I) are scarce. When present, they occur as euhedral to subhedral crystals of several hundred µm generally showing the pericline/tartan twinning. In pegmatitic zones from the

border, very large K-feldspar phenocrysts (e.g., Fig. 2b) of a few mm to several cm in size contain numerous inclusions of albite (10-50 µm) and less frequently of mica.

Li-bearing phosphates (Li-P_I) from the amblygonite-montebrasite series (Michaud et al., 2020) occur either as large twinned euhedral phenocrysts up to 1 mm in size or as smaller subhedral crystals. Two generations of disseminated cassiterite are present (see details more details in Michaud et al., 2020). The first (Cst_I) corresponds to euhedral crystals showing growth zonation. Most are between 10 and 40 µm and closely associated with Li-P_I. The largest crystals, up to 1 mm, contain inclusions of twinned Li-P_I. The second (Cst_{II}, Fig. 3e) occurs as large interstitial crystals of several hundred µm surrounded by albite, i.e., invading the albitic matrix. Cst_{II} contains zoned Mn-columbite-tantalite inclusions (CT_{II}). CT_I, the earliest columbite-tantalite generation, forms disseminated subhedral Mn-columbite crystals of several tens of µm, black in polarized light and strongly zoned in BSE images.

4.2. Intragranitic veins

Essential petrographic features and mineral assemblages are summarized in Table 1. As mentioned in section 2, three types of veins have been distinguished on the basis of geometrical, structural and mineralogical criteria (see details in Michaud et al., 2020). All veins are emplaced within the intrusion and they lack continuation in country rocks. No metasomatic transformation of the granite is apparent at vein margins (e.g., Fig. 2e; f). Type I intragranitic veins consist of N072°E, on average, subvertical veins. Millimetric to pluricentimetric in size, they are made of an alternation of elongated quartz, K-feldspars and Li-phosphates crystals growing perpendicularly from margins to the core of veins. This texture is typical of extensional syntaxial veins (Fig. 2e; Michaud et al., 2020). Most quartz (Qtz_{IV}) and K-feldspars (Kfs_{II}) form anhedral crystals nearly continuous across the vein. Li-phosphates (Li-P_{II}) grow as discontinuous elongate crystals ranging from several tens µm to several mm. Type II intragranitic veins consist of N060°E (on average) subvertical extensional veins composed of massive quartz (Qtz_V) and scarce subhedral Li-phosphate crystals (Li-P_{III}). Last, Type III intragranitic veins consist of subvertical shear veins striking to N090-110°E. They display various mineralogical assemblages. The first and most common assemblage is composed of quartz

(Qtz_{VI}), K-feldspars (Kfs_{III}) and Li-phosphates (Li-P_{IV}) with variable amounts of wolframite (Wf) appearing as euhedral crystals of several hundred µm. The second assemblage only includes subhedral Li-phosphate crystals of several hundred µm and wolframite (Wf) showing a patchy texture. These wolframites contain inclusions of exsolved Mn-columbite (Ct_{III}). A third and last type of assemblage, encountered in only one vein, consists of euhedral quartz of several hundred µm, large euhedral wolframite crystals and minor cassiterite (Cst_{III}). In the granite at vein margins, snowball Qtz_I are partially to entirely replaced (pseudomorphosis) by a new generation of strongly zoned quartz in cathodoluminescence (Qtz_{VII}, Fig. 3f).

5. GEOCHEMICAL RESULTS

5.1. Bulk rock compositions

The 7 new analyses of the granitic facies yield quite homogeneous compositions (Table A.2). Major elements show relatively small variations (68-70 wt% SiO_2, 17.5-18.5 wt% Al_2O_3, 4.5-6 wt% Na_2O, 2.5-4 wt% K_2O, Fig. 4a; b). Granite analyses at vein margins do not differ from away from the veins but, for the border units, data are less grouped (Table A.2). Al_2O_3 extend to higher and SiO_2 to lower concentrations than in the granitic facies; Na_2O (and K_2O) are quite dispersed (Fig. 4a, b). This variability is consistent with border units being on average more feldspar- and mica-rich than the granitic facies and with modal concentrations of K-feldspar and albite being different between aplitic-pegmatitic and aplitic rocks. Concerning the minor elements, FeO_t concentrations are uniformly low, reaching 0.57 wt% maximum in the micaceous facies. The CaO concentrations are also generally low although values can exceed 1 wt% in the border facies (Table A.2). MnO occurs at << 0.1 wt% levels and TiO_2 and MgO are both below detection. In contrast, the P concentrations are very high in the different facies (mostly in the 1.5-2 wt% P_2O_5 range, Table A.2, Fig. 4c). F is mostly between 0.2 and 0.4 wt% (exceptionally up to ~0.6 wt% in the micaceous facies) but lower than in other RMGs (e.g., Beauvoir, Cuney et al., 1992; Raimbault et al., 1995, Fig. 4e). For the other fluxing elements, concentrations are low (< 100 ppm) for B and elevated (in the 1000-2500 ppm range) for Li (Fig. 4e). The Be, Cs, Ga, Nb, Rb, Sn, Ta and W concentrations are generally high (Table A.2). They are quite homogeneous between the different

facies for Cs (25-50 ppm range), Ga (30-45 ppm range), Rb (850-1400 ppm range), more dispersed for Be (15-150 ppm range) and increase with the SiO_2 concentration for Nb (17-89 ppm), Sn (107-1682 ppm) and Ta (19-84 ppm). W (3-59 ppm) shows the largest dispersion, the highest concentrations being found in granite near the northeastern contact of the intrusion (see below). In comparison, Nb, Sn and Ta concentrations at vein margins and away from the veins are generally in the same range (Table A.2). For Li, Nb, Sn and Ta, the lowest values of concentration ranges above are found in the border units (Fig. 4e). Concentrations in compatible elements, Ba, Sr, light rare earth elements (Ce, La), Th and Zr are notably low (Table A.2). S concentrations are below detection (100 ppm) except in one sample (300 ppm) and As is generally < 5 ppm in the granitic facies, reaching concentrations in the 100 ppm range in one border sample and in granite samples from near the northeastern contact of the intrusion.

Samples collected near Type III veins close to the sheared northeastern border of the intrusion are lower in SiO_2 and Na_2O and higher in K_2O, Al_2O_3, CaO and FeO_t than the granitic facies (Table A.2, Fig. 4). Beryllium, Ga, Rb, W and As are all much more elevated (see above) whereas Be, Cs and Sn stay in the same range and Li, Nb and Ta are less enriched than in the granitic facies. These differences are interpreted as local modifications of the granite composition probably induced by the circulation of external fluids near the sheared contact. Another unusual composition in our dataset is the "dyke-like" facies (A8, Table A.2). It shows higher SiO_2 and K_2O and lower Al_2O_3 and Na_2O than the granitic facies (Fig. 4a, b). Trace element concentration trends are similar than in the granitic facies although this sample records the highest concentrations for several elements. This is the case for Rb (1442 ppm), Sn (1960 ppm), Ta (160 ppm), Hf (5.36 ppm) and Th (1.45 ppm, Table A.2).

Overall, the data for the Argemela granitic facies fit the definition of a PHP RMG (Linnen and Cuney, 2005), being highly peraluminous (A/CNK = 1.2 - 1.7, mean value = 1.4), felsic and strongly enriched in P, fluxing and rare elements. The new analyses for the granitic facies (Table 2; A.2) agree with the older data (Charoy and Noronha, 1996) and stress the similarity between Argemela and major element compositions of others PHP RMGs, such as Beauvoir (Raimbault et al., 1995; Fig. 4a, b). Concerning the trace elements, the new and the older data broadly agree for Ga, Nb, Ta, Zr, Hf, W, B but the Li, Rb, Cs concentrations in Charoy and Noronha (1996) are significantly higher and the Sn concentrations lower than in this study (Fig. 4e, f). The Argemela border facies, although less peraluminous (A/CNK = 1.1 - 1.3, mean value = 1.2) and with lower Li

and rare metal concentrations than the granite facies, has P concentrations also in the range of PHP RMGs (Fig. 4c). The "dyke-like" facies represents the evolved end-member in the whole-rock database, similar to the "ball like" facies (Charoy and Noronha, 1996; Fig. 4). Geochemical indicators (Nb/Ta, Zr/Hf) indicate that the evolution from the border, the granitic to the "dyke-like" facies is progressive. Whole-rock Nb/Ta decrease along with Zr/Hf (Fig. 4d) as found in other RMGs (Raimbault et al., 1995).

5.2. Mineral compositions

Micas. Major and trace element analyses of the different mica generations are given in Tables A.3 and A.4, respectively. In the binary Mg-Li - Fe_t+Mn+Ti+Al^{IV} diagram (Fig. 5; Tischendorf et al., 1997), Ms_I plot mainly in the muscovite field with a slight shift toward the phengite, Li-phengite and Li-muscovite fields. As Ms_{II} can be difficult to distinguish from Ms_{III}, both mica types are plotted with the same symbol, falling exclusively in the muscovite field. Mica major element compositions differ little between the $Ms_{I\text{-}II\text{-}III}$ generations although a general evolution toward pure muscovite from Ms_I to $Ms_{II\text{-}III}$ can be noted (Fig. 5a, b). Ms_{IVa} and Ms_{IVb} show a greater scatter which might be due to their patchy texture (Fig. 3d). The two do not exactly overlap, Ms_{IVa} plotting in the muscovite, phengite, Li-muscovite to Li-phengite and Ms_{IVb} in the Li-muscovite, Li-phengite, zinnwaldite to lepidolite fields (Fig. 5a). Therefore, Ms_{IVa} appears as intermediate between compositions of $Ms_{I\text{-}II\text{-}III}$ and Ms_{IVb}. Overall, $Ms_{I\text{-}II\text{-}III}$ are Li-poor dioctahedral micas and Ms_{IV} Li-rich trioctahedral micas. Compositions of mica cores from Charoy et al. (1995) are similar to the $Ms_{I\text{-}II\text{-}III}$ group from this study but rims plot outside the Ms_{IVa} and Ms_{IVb} domains (Fig. 5a). In a ternary M2+ - Li - Al diagram (not shown), rims from Charoy et al. (1995) plot close to trilithionite on the muscovite - trilithionite join and so have lower M2+ than Ms_{IV} from this study.

Chemical zonation in micas from the granitic facies are detailed on a representative example (Fig. 3c; 6). The major element zonation from Ms_I, Ms_{II} to Ms_{III} is little marked (Fig. 5b) and Fe concentrations decrease from core to rim. Concerning the trace elements, Li, Nb, Ta and Sn (to a lesser extent) decrease from core to rim, whereas Rb, Cs (not shown) and Mn are less variable. F is quite constant and B is the only element with concentrations increasing from core to rim. All elements except W pass through a maximum in the Ms_{Ib} - Ms_{IIa}

zone (Fig. 6). The same type of zonation is observed in $Ms_{I-II-III}$ from the border unit (Michaud, 2019). Plotting all mica compositions, a decrease of the Nb/Ta ratio (from 15-11 to 2) is observed from core (Ms_I) to rim (Ms_{II-III}), accompanied by a decrease in Li and an increase of the Mn/Fe ratio (from ~0.1 to more than 0.4, Fig. 7a, b). This evolution is associated with relatively small changes of the K/Rb ratio and Cs concentrations (Fig. 7c). Note that muscovites from the border unit extend to higher K/Rb when compared to the granitic facies. Figure 7 also stresses the contrast in trace element compositions and evolutions between Ms_{IV} on the one hand and $Ms_{I-II-III}$ on the other hand. From Ms_{IVa} (granitic facies) to Ms_{IVb} (border units), the decrease of the Nb/Ta ratio (down to < 1) is accompanied by a strong increase in Li and a decrease of the Mn/Fe ratio (from 0.6 to ~0.2) that goes along with decreasing Al_2O_3 (from ~36 to < 20 wt%, Fig. 7a, b). This evolution is associated with a marked increase in Cs concentrations (up to > 1000 ppm) with slightly decreasing K/Rb (down to 10, Fig. 7c).

Quartz. Of the seven quartz generations recognized, four occur disseminated in the granite (Qtz_I, Qtz_{II}, Qtz_{III} and Qtz_{VII}) and three are from intragranitic veins (Qtz_{IV}, Qtz_V and Qtz_{VI}). The trace element data are given in Table A.5 and illustrated on Fig. 8 and 9. In the granitic facies, the zonation from cathodoluminescence imaging on Qtz_I crystals is weakly marked chemically (Fig. 8a) and so only core-rim relations are detailed below. Cores are slightly enriched in Al (1300-2050 ppm), Rb (7-26 ppm), Li (50-72 ppm), B (10-17 ppm) and Sn (0.10-0.34 ppm) compared to rims (Al: 640-1010 ppm; Rb: 1.4-5.3 ppm; Li: 25-44 ppm, B: 4.7-6.4 ppm and Sn mostly between 0.10 and 0.14 ppm, Table A.5). For most trace elements, concentrations in Qtz_{Ib} (rim) are similar to Qtz_{Ia} (core) except for Ge, higher in Qtz_{Ib} (10.8 ppm) than in Qtz_{Ia} (<3-7 ppm, Fig. 7b). In the micaceous part of the border facies, interstitial Qtz_{III} is depleted in Al (460-700 ppm), Li (11-13 ppm), Rb (3.2-7.8 ppm) and Sn (0.10-0.16 ppm) compared to early Qtz_I (Al ~1520 ppm, Rb: 13-13.7 ppm, Li: 36-44 ppm, Sn ~0.3 ppm, Fig. 8b).

In comparison with quartz disseminated in the granite, quartz from intragranitic veins show more variable trace element signatures (Fig. 8c, Table A.5). For the Type I intragranitic veins, Qtz_{IV} at 1 and 2 mm from the margin (i.e., the two first points in Fig. 8c) have trace element contents (Al: 1160-1390 ppm, Rb: 3.4-5.2 ppm, Li: 27-36 ppm) similar to Qtz_I. However, in the centre of the vein (Fig. 8c), the data reveal a significant decrease of Al (95-254 ppm), Li (3.8-12.1 ppm) and Rb (0.2-0.8 ppm) contents. A slight increase in Sn (0.11-0.16 ppm) is also observed when compared to concentrations near the margin (Sn ~0.09 ppm). For Qtz_V from the Type II intragranitic veins, data are available only in the centre of the vein. Al (50-190 ppm), Rb (0.07-0.1

ppm), Li (0.4-18.8 ppm) and Sn (0.08-0.11 ppm) are very low (Table A.5), similar to Qtz_{IV} from the middle of the vein and even lower for Al and Rb. For Qtz_{VI} (Type IIIa intragranitic veins), the Al, Li and Rb contents strongly decrease with increasing distance from the vein margin as found for the Type I. The data close to the margin reveal relatively high Al (435-844 ppm), Li (28-42 ppm) and Rb (2.95-4.1 ppm) contents. Away from the vein margin, trace element concentrations are very low (Al: 65-75 ppm, Li: 0.8-1.7 ppm). Compositions of all quartz generations are plotted together for comparison (Fig. 9). Data emphasize the compositional contrast between, on the one hand, quartz disseminated in the granite (Qtz_{Ia}, Qtz_{Ib}) and, on the other hand, quartz crystallizing in the centre of intragranitic veins (Qtz_{IVcore}, Qtz_{V} and Qtz_{VIcore}). Early Qtz_{I} from the border facies and quartz in the granite at the margins of Type I and III veins (Qtz_{IV} and Qtz_{VI} margin) plot in the disseminated quartz domain together with Qtz_{Ia} and Qtz_{Ib} compositions. Conversely, Qtz_{VII} (recrystallized quartz in the granite near Type III veins) has very low trace element contents and plots together with quartz from the centre of intragranitic veins. Overall, the data define a trend of systematically decreasing Al, Li, Rb concentrations from disseminated quartz to the vein quartz. In comparison, B, Sn and Ti concentrations are relatively constant for all quartz generations (Table A.5).

K-feldspars. Major and trace element compositions of K-feldspars (Kfs_{I} disseminated in the granite, Kfs_{II} and Kfs_{III} from Type I and III intragranitic veins) are listed in Table A.6 and A.8 respectively. K-feldspars contain negligible An, from 0 to 0.6% but significant Ab, up to ~7%. Most Kfs_{I} in the granitic and border facies (i.e., apart from two analyses, 1.3-2 % Ab), have Ab (3.8- 6.6 %) higher than K-feldspars in intragranitic veins (0.4-3 %). Ab also roughly decreases from Kfs_{II} to Kfs_{III}. K-feldspars contain up to ~0.8 wt% P_2O_5, the highest values being found in the border facies. In Kfs_{I}, Rb contents are generally quite high (in the several 1000 ppm range) but extremely high concentrations, at the wt% level, are also found (24712 ppm, Table A.7). Cs covers a large range from 71 to > 2000 ppm. Rb and Cs are strongly correlated and the Rb-enriched analyses are also unusually high in Cs (2159 ppm, Table A.7). Ba concentrations never exceed 40 ppm. In Kfs_{II} and Kfs_{III}, the Rb contents have lower maximum values than in Kfs_{I} although they stay elevated (4000-7800 ppm), slightly decreasing from Type I to III veins. Cs concentrations can be locally high (350-480 ppm range in Type I veins) progressively decreasing as for Rb. The Ba contents are similar to much higher (up to 194 ppm) in Kfs_{II-III} than in Kfs_{I}. Sn (from below detection to 31 ppm), Li (18-69 ppm), Ge (from below detection to 18 ppm) generally decrease from Kfs_{I} to Kfs_{II} and Kfs_{III}.

Albite. Albite crystals have been only analysed for major elements (Table A.8). All compositions are close to the albite end-member. Ab_{Ia} (inclusions in Qtz_I cores) show Al (1.01-1.06 apfu), P_2O_5 (0.33-0.83 wt%) and An (0.41-0.91 %) slightly higher and Or (0.41-0.72 %) slightly lower than Ab_{Ib} (inclusions in Qtz_I rims; Al: 1.01-1.04 apfu; P_2O_5: 0.01-0.4 wt%; An: 0-0.3 %; Or: 0.32-0.87 %). Ab_{II} (matrix of the granitic facies) compositions do not differ appreciably (Al: 0.99-1.02 apfu; P_2O_5: 0-0.34 wt%; An: 0-0.3 %; Or: 0.4-0.87 %) from Ab_{Ib}. $Ab_{IIaplite}$ plot in the same range than Ab_{II} from the granitic facies while Ab_{IIpeg} shows only slight differences with the other compositions.

Li-phosphates. Li-phosphates analysed include isolated crystals disseminated in the granite (Li-P_{Ia}), inclusions in disseminated cassiterite (Li-P_{Ib}) and crystals in the three types of intragranitic veins (Li-P_{II}, Li-P_{III} and Li-P_{IV}). Li-phosphates have a restricted major element variability with F ranging from 3.2 to almost 5.4 wt% (which corresponds to 59 to 76 % montebrasite in the montebrasite-amblygonite solid solution, Michaud et al., 2020) and Li contents from ~47 400 to ~51 000 ppm (Table A.9). Be, B, Ti, Mn, Fe, Ga, Nb, Sn, Ba, Sr, Ta, U show concentrations systematically above detection while other elements do not enter the montebrasite structure (Table A.9). Notable points include the low Nb/Ta of Li-phosphates and their Sn contents. In the granitic facies, the Nb/Ta ratio increases from Li-P_{Ia} (0.02-0.03) to Li-P_{Ib} (0.24-0.46) most probably because Ta is preferentially than Nb incorporated in host cassiterite (see below). Sn contents can be quite high, up to ~90 (isolated crystal) and ~140 ppm (inclusion in cassiterite). In the intragranitic veins, the Nb/Ta ratio (0.02-0.20) is lower in the granite and the highest values are found in crystals from the Type III veins. Sn concentrations are elevated (71-179 ppm, Table A.9).

6. STABLE ISOTOPE RESULTS

O and H isotopic compositions have been determined for quartz and a few analyses are available for muscovite. The analysed quartz include Qtz_I from the granitic facies, Qtz_{I-III} from the micaceous facies and $Qtz_{IV-V-VI}$ from each generation of intragranitic veins. The analysed muscovites are Ms_{I-III} from the granitic and the micaceous facies (see Table 1 for textural details).

6.1. Oxygen isotope data

The oxygen isotope data are given for both quartz and muscovite in Table 3 and shown in Fig. 10. Muscovite from both the granitic and micaceous facies yield identical $\delta^{18}O$ (11.7‰). In contrast, quartz (Qtz_I and $Qtz_{I\text{-}III}$) yields different $\delta^{18}O$ values, +13.7 and +14.5‰ in the same two facies respectively. The highest value found in the micaceous facies probably reflects analysis of a mixture between Qtz_I and Qtz_{III}. The quartz-muscovite O isotope fractionation factor (Δ_{QtzMu}) is 2 when calculated for Qtz_I of the granitic facies and 2.8 for $Qtz_{I\text{-}III}$ of the micaceous facies. Using the thermometric equations of Zhang et al. (1989) and O'Neil and Taylor (1969), the two Δ_{QtzMu} values give temperatures of isotopic equilibration between quartz and muscovite of ~500 and ~800°C respectively.

For quartz in intragranitic veins, $\delta^{18}O$ range from +14.5 to +16‰, progressively increasing with the vein type in the order $Qtz_{IV} < Qtz_V < Qtz_{VI}$ (from the earliest to the latest). Quartz from Type I veins (Qtz_{IV}) have $\delta^{18}O$ of +14.5 and +15‰, the lowest value being identical to $Qtz_{I\text{-}III}$ in the micaceous facies. Qtz_V from Type II veins has a $\delta^{18}O$ of +15.6‰ while Qtz_{VI} (Type III) have the highest $\delta^{18}O$ values, +15.5‰ and +15.9‰.

6.2. Hydrogen isotope data

Hydrogen isotope data are given in Table 4 and shown in Fig. 11. Muscovites of the granitic facies contain 3.85 and 3.87 wt% H_2O respectively and they yield δD of -64.7‰ and -65‰ while, in the micaceous facies, muscovites have slightly lower H_2O contents (3.57 and 3.55 wt%) and δD (-66.9‰ and -67.4‰; Fig. 11a). For fluids trapped in quartz (i.e., δD of the fluid), δD range from -20.2 to -52.1‰. δD of fluids in Qtz_I from the granite range from -26.1 to -48.5‰ (7 analyses) with a mean value of -35.4 ± 7‰ (Table 4; Fig. 11b). The micaceous facies yield fluid in quartz δD values of -39.4 to -46.5‰ (n=3) with a mean value of -41.9 ± 3‰, so higher than for the granitic facies. Fluids in Qtz_{IV} have δD between -21.2 and -34.9‰ (n=13, mean value of -28.5 ± 4.4‰), fluids in Qtz_V range from δD = -20.2 to -52.1‰ (n=6, mean value of -33.5 ± 12‰) and fluids in Qtz_{VI} yield δD between -25 and -30.9‰ (n=3, mean value of -28.2 ± 3‰). Last, δD of fluids from the Santa

Rita vein quartz (Qtz_{IIISR}) are between -35.3 and -43.9‰ (n=4) with a mean value of -38.9 ± 4‰. Overall, the mean fluids in quartz δD values are lower in the granitic and micaceous facies than in the intragranitic veins apart from the Santa Rita vein.

7. DISCUSSION

7.1. Crystallization of the Argemela RMG along the magmatic-hydrothermal transition

Several lines of evidence demonstrate that the Argemela granite results from the crystallization of a highly evolved rare-metal magma (see also Charoy and Noronha, 1996). The subvolcanic texture (Fig. 2a) exhibited by the granitic facies is a typical feature of RMGs and indicates crystallization at shallow levels (e.g., Müller and Seltmann, 1999). The presence of a two-feldspars, muscovite plus quartz mineral assemblage calls for a parental granitic melt and the bulk granite composition (strongly peraluminous with high P_2O_5, Li, Sn and rare metals concentrations) indicates that the Argemela intrusion is a representative example of a PHP RMG. Unidirectional solidification textures (Fig. 1b), such as observed in the border unit are typical features of pegmatite wall zones and are generally attributed to the effect of liquidus undercooling (e.g., Uebel, 1977; London 2009; London, 2014). Given the conditions (greenschist facies) in the host rocks, undercooling was likely enhanced along the margins by the large temperature contrast with the Argemela magma. The complex zonation of the border unit might then be explained by different degrees of undercooling as heat flow out of the intrusion. Although a detailed interpretation of this unit is beyond the scope of this paper, the less fractionated chemistry of the border (i.e., lower whole rock Sn, Li; slightly lower Rb and higher Nb/Ta; higher K/Rb in $Ms_{I-II-III}$; Fig. 4; 7) when compared to the granitic facies suggests that the former crystallized first. Internal differentiation proceeded inwards through progressive crystallization of the intrusion at its emplacement level (e.g., London, 1990; similar to internal differentiation in a pegmatite).

The main constitutive minerals of the intrusion - Qtz_I, Ms_{I-II}, Kfs_I and Ab_{I-II} - are euhedral without apparent dissolution or recrystallization (e.g., Fig. 3a, c). This strongly suggests that crystals were able to grow freely in broadly the same crystallization environment. Zoning patterns observed in Ms_{I-II} and Qtz_I, the euhedral

habit of crystals and presence of zonally disposed inclusions (e.g., albite in Qtz_I, Fig. 3a) strengthen this interpretation (Müller and Seltmann, 1999) and calls for a primary igneous origin (i.e., Holness et al., 2018). In a convective or rising melt, one would expect to see inherited cores and/or resorption features, indicating distinct crystallization environments (e.g., Breiter et al., 2005). Accessory minerals including Cst_I, closely associated with Li-P_I, and CT_I exhibit zoning patterns similar to Qtz_I and Ms_{I-II}, which strongly suggests their crystallization at the magmatic stage (see Michaud et al., 2020). Strong enrichments in Li, Sn, Nb, Ta and W in mica cores (i.e., typically in Ms_I; e.g., Fig. 6) and in Li and Al in Qtz_I (Fig. 8a) strongly suggest that the parental melt was enriched in these elements, consequently sourced in the intrusion. Enrichments in rare elements in quartz, together with a depletion in Ti, are characteristic of highly evolved and flux-enriched magmas crystallizing at low temperatures (e.g., Breiter and Müller, 2009; Breiter et al., 2013; Müller et al., 2018). High Li and Al concentrations in the melt are necessary for their incorporation in the quartz lattice (Breiter et al., 2017; Müller et al., 2018) even if the correlation between Al in quartz and peraluminous character is still debated (Breiter and Müller, 2009). Albites with near end-member compositions (i.e., Ab > 96%; Table A.8), as also found in other RMGs (e.g., Cuney et al., 1992; Breiter et al., 2017; Borska and Kubiš, 2018; Zhu et al., 2018), have been often interpreted as secondary albitized compositions (e.g., Schwartz, 1992). However, a primary magmatic origin is also possible for near end-member albite (Lukkari and Holtz, 2007). Ab_{Ia}, included in snowball quartz cores, are enriched in P_2O_5, An and Al_2O_3 (i.e., the correlation between Al and P follows the substitution mechanism: Al + P = 2 Si, see below) while Ab_{Ib} in external zones are relatively depleted in these elements, which could indicate syn-crystallization with micas and/or montebrasite. Kfs_I are also quite enriched in P_2O_5 (Simpson, 1977; London et al., 1990; 1999), which, together with a similar enrichment in early albite, requires high P contents in the parental melt (from 0.2 to 0.7 wt% P_2O_5, London et al., 1999), a key characteristic of PHP magmas. These K-feldspars contain significant amounts of Ab interpreted as an inheritance from their early magmatic compositions.

Fluids were present during the crystallization of the Argemela intrusion as highlighted by the fluid inclusion (FI) study of Lima et al. (2019). The occurrence of primary FI in rims of "QtzI" and "QtzII" (most probably corresponding to our Qtz_{Ib} or Qtz_{III}) and their CO_2-bearing chemistry suggest that fluid exsolution started early. This is consistent with textures of Ms_{III} (Fig. 3c) and Cst_{II} (Fig. 3e), which, similarly to Qtz_{III} (Fig. 3b), are interpreted to crystallize in a magma with an exsolved fluid phase present. These phases occur as

interstitial crystals, overgrowing older crystals or isolated, and they invade the matrix. Their interstitial morphologies strongly contrast with the euhedral habits of the earlier Qtz_I, Ms_{I-II}, Kfs_I and Ab_{I-II}. Their low dihedral angles against adjoining euhedral grains - especially for Qtz_{III} and Cst_{II} - suggest that they precipitated, at least partially, from a melt phase (Holness et al., 2018), infilling the space left by the crystallization of the main assemblage. The evolution of mineral morphologies thus suggests that crystallization evolved from a free space to a constrained environment. This textural evolution is associated with marked variations in trace element concentrations. From M_{I-II} to Ms_{III}, Fe, Li, Sn, Nb, Ta, W significantly decrease while B increase (Fig. 6). Similarly, Li, Al and Sn concentrations decrease from Qtz_I to Qtz_{III} while B slightly increases (Fig. 8b). The association of Ta-rich Cst_{II} and Mn-, Ta-rich CT is representative of fluid-melt interactions late in the crystallization of the intrusion, where Mn is transported in the fluid and Ta remains in the residual melt (see 7.2 and McNeil et al., 2020).

The intragranitic vein system is a clear marker of the end of the magmatic stage and of the transition toward hydrothermal processes as already emphasized in Michaud et al. (2020). The intrusion is interpreted as fully solidified at that stage and further crystallization is confined to within the veins. The mineralogical mode of the vein system evolves from quartzo-feldspathic (Type I) to essentially quartz-bearing (Type II and III). Experimental fluids at equilibrium with granitic melts at low pressures ($\leq$ 200 MPa) are dominated by Si and alkali; they contain only some Al and their normative compositions are dominated by quartz with only a small proportion of feldspathic components (e.g., Burnham, 1967). If Li, B, F or P are present, proportions of dissolved feldspathic components increase (Pichavant, 1981; Sowerby and Keppler, 2002; London, 2014). The mineralogical mode of the vein system at Argemela is globally consistent with compositions of experimental igneous fluids. Type I veins can be interpreted to represent the crystallization/condensation of the minor quartzo-feldspathic fraction dissolved in the fluid and Type II and III veins of the dominant quartz fraction. The chemistry of mineral phases in veins demonstrate a genetic link with the magmatic evolution. Trace element (Li, Al) concentrations in Qtz_{IV} and Qtz_{VI} close to vein margins (since data for Type II veins are limited) are similar to the early magmatic Qtz_I. From Type I to III veins, the overall decreasing evolution of Li, Al and Ge in quartz (Fig. 9) and of Li, P and Ba in alkali feldspar (Table A.6) can be explained by the mobilization of Al, Li and P from the fluid to form montebrasite and a decrease of the Ge solubility in the fluid with decreasing temperature (Pokrovskii and Schott, 1998). High concentrations in the elements above, plus the significant

concentrations in Sn, Nb, Ta and W revealed by the bulk rock analysis of a Type I vein (Table A.2), highlight the ability of the fluid to carry rare elements despite macroscopic ore minerals being absent. The bulk rock analysis of a Type III vein (Table A.2) is much less enriched in rare elements than the Type I, which, likely results from the crystallization of Cst_{III}, Wf and CT_{III} in Type III veins depleting the fluid in the corresponding metals.

The patchy texture of Ms_{IV}, invading earlier micas in the border unit (Fig. 3d), and their strongly differing chemical signature (i.e., zinnwaldite to lepidolite compositions; Fig. 5; 7) call for a late metasomatic origin. The Li- and F-rich chemistries of Ms_{IV} are inconsistent with an origin involving fluids external to the intrusion. Therefore, crystallization of Ms_{IV} most probably marks a local and late Li-rich subsolidus crystallization stage that partially transforms and replaces earlier mineral assemblages. It is worth emphasizing here that metasomatic transformations of early phases are of minor importance at Argemela and restricted to the border facies. Although of limited extension (i.e., along the northeastern sheared border of the intrusion), external contamination is marked by the crystallization of sulphides, such as arsenopyrite (Fig. 2g), vivianite and stannite, the latter replacing cassiterite in late little fractures or disseminated mainly around/inside Type III veins. Indeed, the S-rich mineral assemblage is viewed as an indication for the involvement of fluids external to the intrusion since the granite is very poor in S (whole S contents mostly below 100 ppm, Table A.2).

In summary, crystallization of the Argemela intrusion involves three main stages, magmatic, magmatic-hydrothermal and early hydrothermal (Fig. 12). The magmatic stage corresponds to the crystallization of major phases and partly of accessory/minor minerals. As the proportion of fluid within the intrusion increases, specific textures develop and a largely crystallized magma coexisting with a magmatic fluid is obtained (magmatic-hydrothermal stage). The early hydrothermal stage, contemporaneous to postdating final granite solidification, corresponds to the infilling of the intragranitic vein system and to the crystallization/condensation of the silicate fraction dissolved in the fluid. Late stages include limited metasomatic replacement of earlier minerals and local influx of external fluids.

7.2. Geochemical modelling

Chemical evolution from core to rim in muscovite was modelled geochemically to identify fractionation mechanisms and evaluate the role of the fluid phase in the distribution of metals. The approach and models are detailed in the Appendix together with mass fractions, mineral/melt and fluid/melt partition coefficients. Modelling focused on simulating the variations from Ms_I to Ms_{III}, excluding compositions of Ms_{IV}. Trace element zonations in muscovite are of the same type in the granitic than in the border facies except rims being slightly depleted in Mn in the former and slightly enriched in the latter (Fig. 6; 7 and Table A.4). In the analysed muscovite of the granitic facies, the anomalous character of the Ms_{IIb} point should be noted, being very high for Rb, Cs and very low for B, Nb, Ta, Sn, W and, consequently, only smoothed variations from Ms_{IIa} to Ms_{III} were modelled (Fig. 6).

Li, Sn, Nb and Ta are all characterized by slight initial enrichments and then depletions as muscovite crystallizes (Fig. 6). These elements have bulk partition coefficients (D = sum of mineral/melt partition coefficients weighted by the mass fraction of the respective mineral, e.g., Hanson, 1978) all < 1 in the Argemela magma. With mass fractions and mineral/melt partition coefficients ($Kd_{mineral} = C_{mineral} / C_{melt}$) summarized in Tables A10 and A11 respectively, D values range from 0.07 for Sn, 0.39 for Li, 0.57 for Ta to 0.60 for Nb (n.b., Ta and Nb are both compatible in cassiterite). Consequently, all elements above should increase in melt and muscovite during fractionation, which is observed but only from Ms_{Ia} to Ms_{Ib} (Fig. 6). If a fluid phase is present, the fluid mass fraction and fluid/melt partition coefficients ($Kd_{fluid} = C_{fluid} / C_{melt}$) come into play in the calculation of D. For elements preferentially partitioned toward the fluid (i.e., $Kd_{fluid} > 1$), less marked enrichments or even depletions (depending on the Kd_{fluid} value) can be obtained during fractionation. For example, for a constant fluid mass fraction of 0.05, a Kd_{fluid} of 8 for Nb yields D = 1 (vs. D = 0.6 under fluid-absent) thus suppressing Nb enrichment. The same result (D = 1) is obtained with a Kd_{fluid} of 9 for Ta (vs. D = 0.57). However, these two Kd_{fluid} exceed by ~1 order of magnitude the range commonly accepted for Nb and Ta (0.1-1, Table A12). Therefore, the Nb and Ta depletions observed from Ms_{Ib} to Ms_{III} (Fig. 6) are unlikely to be controlled by fluid partitioning. Below, the behaviour of Li, Sn, Nb and Ta is modelled by combining fractionation and saturation models for montebrasite, cassiterite and columbite-tantalite (Appendix; Janousek et al., 2016). Results for Sn are illustrated on Fig. 13a. The modelling reproduces satisfactorily the initial concentration increase noted in muscovite until crystallization of cassiterite starts at F ~ 0.5. For more advanced

fractionation (F < 0.4), the muscovite Sn concentration becomes controlled by the variation of cassiterite solubility with decreasing temperature and a final Sn concentration (157 ppm, F = 0.05) in the range of Ms_{III} rim concentrations (110-183 ppm, Table A.4) is reached. During this evolution, the calculated proportion of cassiterite crystallized is 0.11 %, close to the natural proportion (0.1 %, Appendix and Table A10). For Li, saturation in accessory phosphate occurs earlier (at F = 0.7-0.8) and the calculated proportion of montebrasite is 3.3 % (2.9 % in the granite, Appendix and Table A10) although the final muscovite concentration (1137 ppm) is higher than analysed in Ms_{III} (378-684 ppm, Table A.4). Columbite-tantalite saturation is reached late (at F = 0.3 and 0.2) for Nb and Ta respectively. Final concentrations in muscovite are 39 ppm Nb and 6 ppm Ta (vs. 14-30 Nb and 4-5 ppm Ta in Ms_{III}, Table A.4) and the calculated CT proportion (0.02 %) is in the same range as the natural proportion (0.01 %, Appendix and Table A10). Therefore, and although the saturation models are quite simple and the agreement with the analytical data no better than reasonable for some elements, the main features of element zonations observed in muscovite are reproduced. The Li, Sn, Nb and Ta variations all result from (1) an early incompatible behaviour during crystallization of the intrusion until (2) a minor/accessory carrier phase saturates and (3) concentrations in the melt then follow the solubility of the saturating phase, progressively decreasing as temperature decrease.

At the exception of Mn in columbite-tantalite, the other modelled elements are not essential structural constituents in minor or accessory phases, and they follow classical trace element behaviour. W is compatible in cassiterite and columbite-tantalite, occurring at wt% levels in CT from Type III intragranitic veins (Michaud et al., 2020). The bulk D for W (calculated under fluid-absent conditions) is 0.31 and consequently an increase of the W concentration in muscovite is expected during crystallization. However, the behaviour of W is strongly affected by the presence of a fluid phase because the Kd_{fluid} for W is >> 1, with values of 10 or higher having been recently found experimentally (Schmidt et al., 2020). If a Kd_{fluid} = 15 (Table A.12) is assumed, the bulk D for W increases to > 1 (vs. 0.31 under fluid-absent) and the three fluid-present models tested all lead to W depletion in muscovite during fractionation (Fig.13b). The final W concentrations calculated with the different models (either 2, 13 or 20 ppm, F = 0.05) bracket the range of analysed rim concentrations in Ms_{III} (3-16 ppm, Table A.4). Therefore, the progressive depletion of W during muscovite growth reflects transfer of W from the melt toward the magmatic fluid phase as cooling, crystallization and fluid exsolution proceed.

Other elements whose behaviour sensitively depends on fluid/melt partitioning include Mn and B. Mn is incompatible (fluid-absent bulk D = 0.22) but, similar to W, it is partitioned in favour of the fluid (Zajacz et al., 2008; Iveson et al., 2019, Table A.12), which regulates its enrichment in the melt during crystallization. Using the same three fluid-present models as for W, final (F = 0.05) Mn concentrations in muscovite are either 2334, 1876 or 784 ppm, vs. rim concentrations of 295-969 ppm Mn in Ms_{III} from the granitic facies (999 ppm Mn in the border facies, Table A.4). Note that these calculated Mn concentrations are maximum values because late saturation in columbite-tantalite is not incorporated in the modelling. For B, fluid partitioning (Table A.12) does not prevent this element to be strongly concentrated in the melt because of its markedly incompatible character (fluid-absent bulk D = 0.01). Final (F = 0.05) concentrations calculated with the same three fluid-present models as above range from 955, 873 to 610 ppm B, slightly exceeding concentrations in Ms_{III} rims (353-556 ppm B, Table A.4). In comparison, Rb and Cs, with Kd_{fluid} between 1 and 2 (Table A.12), are not significantly influenced by the fluid. These two elements are continuously enriched in muscovite, consistent with their incompatible character (fluid-absent bulk D = 0.23 and 0.01 for Rb and Cs respectively), except the last point in Ms_{III} (Fig. 6). In this respect, large Rb and Cs enrichments occur in Kfs_I (> 1 wt% Rb and > 1000 ppm Cs, Table A.7). This suggests a change of geochemical behaviour for these elements as crystallization proceeds, probably in response to decreasing temperature. This late compatible character of Rb and Cs was accounted for by using fractionation models with increasing D (Appendix, Greenland, 1970), which satisfactorily reproduced the type of zonation and range of Rb and Cs concentrations analysed in Ms_{III}.

To conclude, the trace element variations recorded during muscovite growth allows two fractionation mechanisms to be identified in the Argemela intrusion in addition to crystal fractionation, (1) crystallization of minor/accessory phases, which sequesters Li, Sn, Nb, Ta from the melt and (2) fluid partitioning, which transfers W, Mn, B out of the melt toward the fluid phase. The different rare elements behave remarkably selectively during this evolution governed by the nature of major phases and accessory/minor minerals, and by the fluid/melt partition coefficients. We emphasize that the trace element evolutions modelled in muscovite also occur although less marked in quartz (decrease in Al, Li, Sn, slight increase in B from Qtz_I to Qtz_{III}, Fig. 8b).

7.3. Origin of fluids

7.3.1. The intrusion as the fluid source

Several types of observations constrain the possible origin of the fluids. (1) The aquo-carbonic, N_2-bearing and Cl-poor primary FI in quartz demonstrates that fluids were present during crystallization of the intrusion (Lima et al., 2019). (2) The confinement of quartz veins inside the granite and the fact that both the granite and veins were emplaced in the same deformation regime (Michaud et al., 2020) indicate that fluids come from within the intrusion. (3) No major hydrothermal transformation is observed in the granite at vein margins. Secondary mineral assemblages (i.e., greisens) are absent or minor (Fig. 2e, f) and the granite near the veins only shows slight increases in P_2O_5, Li, Nb and Ta (in comparison, the granite near Type III veins at the northeastern sheared part of the intrusion is more chemically modified). Globally, fluids in the veins were at equilibrium with the solidified granite. (4) Quartz at the margins of Type I and III intragranitic veins have trace element contents very similar to disseminated quartz in the granitic facies (Fig. 8c).

7.3.2. A single high $\delta^{18}O$ fluid

The stable isotope data provide additional constraints. The quartz $\delta^{18}O$ values demonstrate a progressive increase from early magmatic Qtz_I, Qtz_{I-III} in the micaceous facies to Qtz_{IV}, Qtz_V and Qtz_{VI} in intragranitic veins (Fig. 10; Table 3). The lowest $\delta^{18}O$ value in Qtz_{IV} is identical to that in Qtz_{I-III} from the micaceous facies, confirming chemical equilibrium between intragranitic veins and the granite. The $\delta^{18}O$ in intragranitic veins increases opposite to their relative age (i.e., $\delta^{18}O$ Qtz_{IV} < $\delta^{18}O$ Qtz_V < $\delta^{18}O$ Qtz_{VI}). Overall, the $\delta^{18}O$ evolution indicates a progressive change in the magmatic-hydrothermal system with time, which can be interpreted in two possible ways, either (1) progressive cooling of a single fluid or (2) multiple fluids with increasing ^{18}O content.

The first interpretation is supported by the relatively narrow range of H isotopic data (δD = -20.2 to -52.1‰ for fluids trapped in quartz, Fig. 11; Table 4). There is no evidence in our dataset for highly variable δD values as found, for example, in the Panasqueira vein system nearby with δD as low as -130‰ interpreted as the signature of different fluid reservoirs (Kelly and Rye, 1979; Polya et al., 2000). The second interpretation requires multiple ^{18}O-enriched fluids in a range greater than normally expected for meteoric waters (Kelly and

Rye, 1979; Polya et al., 2000). Interaction with meteoric waters would decrease (and not increase) $\delta^{18}O$ as observed on the Beauvoir granite (e.g., Fouillac and Rossi, 1991). Therefore, the alternative appears to be between a unique non-meteoric fluid with high $\delta^{18}O$ and multiple non-meteoric fluids with high $\delta^{18}O$. Additional analyses and a much larger dataset would be needed to test the latter hypothesis and there appears no justification to interpret the progressive $\delta^{18}O$ increase observed at Argemela otherwise than in terms of cooling of a single non-meteoric fluid.

7.3.3. Temperatures and fluid isotopic compositions

$\delta^{18}O$ of fluids in equilibrium with quartz and muscovite have been calculated from the mineral-water equilibrium equations of Zhang et al. (1989) and O'Neil and Taylor (1969) respectively. To do so, temperature must be specified. Isotopic equilibration temperatures of ~500 and ~800°C have been obtained from Δ_{QtzMu} (2 and 2.8) in the granitic and micaceous facies respectively. This temperature interval is large and, moreover 800°C is inconsistent with the upper stability of muscovite in RMG magmas (Scaillet et al., 1995; Pichavant et al., 2016). Below, experimental data on the Beauvoir granite are used to estimate the temperature of coexistence of quartz and muscovite and the solidus of the Argemela granite. Detailed experimental phase equilibria are available for two Beauvoir PHP RMG compositions at 100, 200 and 300 MPa under H_2O-saturated conditions (Pichavant et al., 1987a). Assuming a pressure of emplacement of 150 MPa for the Argemela granite (in the range proposed by Lima et al., 2019), muscovite co-crystallizes with quartz from 650°C down to the solidus (550°C, Pichavant et al., 1987a). For comparison, Lima et al. (2019) estimated a solidus temperature of 500°C for Argemela. Below, the mineral-water calculations were performed at 550, 600 and 650°C.

For these three temperatures, calculated $\delta^{18}O$ of equilibrium fluids are 11.5‰, 12.1‰ and 12.5‰ (Qtz_I), 12.3‰, 12.8‰ and 13.3‰ ($Qtz_{I\text{-}III}$) and, for fluids at equilibrium with muscovite, 12.1‰, 12.5‰ and 12.8‰, respectively (Table 5). These $\delta^{18}O$ values plot within the range (9-13‰) of magmatic waters defined by Sheppard (1977), see also Smith et al. (1996; Fig. 14). However, if the narrower range of magmatic waters $\delta^{18}O$ (11$\pm$1‰) given by Polya et al. (2000) for the nearby Panasqueira system is adopted, most Argemela values plot higher than the range (Fig. 14). δD of fluids in equilibrium with muscovite, calculated at 550°C from O'Neil and Taylor (1969), are -52.2‰ for the granitic facies and -54.4‰ for the micaceous facies. These δD values

constrain the early magmatic signature since water is part of the mica structure and they plot in the range of magmatic waters defined by Sheppard (1977; -40 to -65‰) and Polya et al. (2000; -40 to -80‰). The mean δD value of fluids in Qtz_{I-III} also plots within the magmatic boxes. However, fluids in Qtz_I and in quartz from intragranitic veins have δD higher than magmatic waters, plotting in the field for pegmatites and skarns defined by Alderton and Harmon (1992; see also Smith et al., 1996). The evolution from early magmatic (constrained by muscovite) to hydrothermal (constrained by vein quartz) δD defines a subvertical trend (Fig. 14). Such a trend has been recognized in other similar systems worldwide (Shieh and Zhang, 1991; Bettencourt et al., 2005; Chicharro et al., 2016; Van Daele et al., 2018). For example, in the Dajishan Mine (Jiangxi Province, Southeast China), the fluid δD values increase (at nearly constant $\delta^{18}O$) from the magmatic (defined by minerals from the muscovite granite) to the main Sn-W ore stage (defined by minerals from the veins). In this system, the isotopic compositions of the main ore fluids are interpreted to have equilibrated with the granitic magma at very low water/rock ratios (i.e., granite-buffered fluid compositions, Shieh and Zhang, 1991). The δD signature in the Argemela intragranitic veins is interpreted in an analogous way. Note that such "vertical" δD - $\delta^{18}O$ evolutions have been also attributed to outgassing of earlier fluids from the magma (Taylor, 1986), depletion of late-magmatic fluids in deuterium (Carten et al., 1988), variations linked to fluid-magma isotope effects (Rye et al., 1990) and minor admixtures of meteoric waters (Heinrich, 1990). All these interpretations accept a dominantly magmatic origin for the fluid.

Inverse calculations were also performed as a test of the temperature range (550-650°C) chosen. An average $\delta^{18}O$ value of 12‰ was assumed for the fluid (Fig. 14) and mineral $\delta^{18}O$ and mineral-fluid equilibrium equations were used to solve for temperature. In the granitic and micaceous facies, results using quartz range from 595 to 526°C, 541°C using muscovite (Table 5). These temperatures and the 550-650°C interval defined above partially overlap, thus demonstrating the internal consistency of our temperature-$\delta^{18}O$ calculations and confirming the temperature range. If it is assumed that quartz in intragranitic veins are at equilibrium with the same fluid ($\delta^{18}O$ = 12‰), temperatures of 504°C for the Type I, 454°C for the Type II and 459-437°C for the Type III (Table 5) are obtained. These values reproduce the expected progressive temperature decrease from the final crystallization of the intrusion to the successive episodes of fluid circulation in veins. They are in the same range as temperatures recently suggested for the Panasqueira wolframite-bearing quartz veins (up to 450°C; Codeço et al., 2019).

In summary, the isotopic data demonstrate a clear magmatic origin for the early fluids and granite-buffered signatures for the vein-forming hydrothermal fluids. No addition of external fluids (i.e., metamorphic or meteoric) can be clearly detected from the isotopic data and, so, the intragranitic veins can be considered as the expression of the exsolution of magmatic fluids.

7.4. A model for magmatic fractionation and the magmatic-hydrothermal transition in rare metal granites

The combination of mineralogical, petrographical and geochemical data on Argemela leads to a model for magmatic fractionation and the magmatic-hydrothermal transition, illustrated in Fig. 12. Five main mechanisms are highlighted. (1) Solidification of the intrusion proceeds inward from the border zone, leading to crystallization of the main magmatic assemblage. Closed system differentiation in situ at the emplacement level yields a progressively fractionated residual melt. (2) Magmatic crystallization of accessory/minor (MCMA) rare element carrier phases (cassiterite, columbite-tantalite and montebrasite) follows their saturation in the fractionated melt. (3) The increasing mass fraction of fluid present in the intrusion makes the fluid phase becoming an important fractionating agent and the behaviour of elements follows fluid/melt partitioning. (4) The intragranitic vein system forms by segregation and collection of exsolved magmatic fluids. The evolution of vein geometries from Type I-II to Type III marks a change in the rheological behaviour of the intrusion from slightly ductile to fully brittle. (5) Ore mineral deposition in intragranitic veins takes place from magmatic fluids.

In the model above, a particular role is attributed to MCMA. This fractionation mechanism, quantitatively evaluated for the first time in this study, requires both elevated concentrations in the melt and an incompatible behaviour for the elements considered (Li, Sn, Nb, Ta). Thus, MCMA superimposes on crystal fractionation that has the capacity to enrich the melt in rare elements (Fig. 13a). It yields strongly unusual geochemical signatures for incompatible elements, characterized by depletions with progressive fractionation, the consequence of the negative temperature dependence of accessory mineral solubilities (e.g., Montel, 1993; Janousek et al., 2016). It illustrates that rare metal enrichments are not necessarily amplified during the MHT. At Argemela, Sn, Li, Nb, Ta are progressively depleted during crystallization as a consequence of MCMA but

depletion in the melt is accompanied by sequestration in accessory minerals and, so, primary ore mineral concentrations are constituted. Cassiterite, columbite-tantalite and Li-Al phosphates are common magmatic minerals in RMGs (Cuney et al., 1992; Yin et al., 1995; London et al., 1999) and LCT pegmatites (Raimbault, 1998; Hulsbosch et al., 2014; Kaeter et al., 2018; Hulsbosch and Muchez, 2020) and the model for Argemela should have wide applicability.

The fluid phase has been often considered to control the extraction of elements and their redistribution out of crystallizing magmas (Ballouard et al., 2016; Hulsbosch et al., 2016; Hulsbosch and Muchez, 2020). In this study, the role of the fluid phase has been quantitatively evaluated (Table A11; 12). Element extraction by the fluid is highly selective, being important for some elements and minor for others. W is remarkable as its progressive depletion in muscovite is controlled by partitioning toward the fluid (Schmidt et al., 2020), despite a strongly incompatible behaviour (Fig. 13b). For Mn and B, fluid partitioning regulates the enrichments associated with fractionation (see *7.2*). In comparison, elements, such as Sn, Nb and Ta are not strongly influenced because their fluid/melt partition coefficients are ~1 or less (Table A12). A similar decoupling between the geochemical behaviour of W on the one hand, and Sn, Nb and Ta on the other hand, has been previously noticed (Hulsbosch et al., 2016). This is not to say, however, that the latter elements are not redistributed by the fluid. For example, using a Sn fluid/melt partition coefficient of 1 (Table A12), fluid Sn concentrations of 270-460 ppm are calculated at equilibrium with Ms_{III} (Fig. 13), in the range measured in FI from pegmatites (8-410 ppm, Hulsbosch et al., 2016). For W, analoguous calculations yield a concentration of 20-120 ppm W in the fluid, to be compared with 4-70 ppm W in FI from the Panasqueira vein system (Lecumberri-Sanchez et al., 2017), and with 3-575 ppm (Hulsbosch et al., 2016) and 167 +/- 92 ppm W (Sirbescu et al., 2013) in FI from pegmatites. These different figures overlap, both for Sn and W, which gives confidence in our ability to constrain rare metal concentrations in magmatic-hydrothermal systems.

Crystallization of ore minerals in the Argemela intragranitic vein system shows that Sn, W deposition is not restricted to late hydrothermal stages but can occur earlier, at higher temperatures and in direct relation with magmatic fluids. Wolframite precipitates as hübnerite in Type III veins only (Michaud et al., 2020). This contrasts with Sn, which saturates early to form magmatic cassiterite. Precipitation of macroscopic cassiterite is observed also in Type III veins (Michaud et al., 2020), yet an elevated bulk Sn concentration (578 ppm), slightly higher than concentrations calculated above for magmatic fluids (270-460 ppm Sn), has been analysed

in a Type I vein (Table A.2). This bulk Sn concentration is within the range of the solubility of cassiterite at 500°C (from ~500 to 970 ppm Sn for a 0.02 molar HCl fluid between HM and NNO, Schmidt, 2018) suggesting that microscopic cassiterite grains are present in Type I veins. Therefore, Sn is mostly deposited within the intrusion and in early hydrothermal veins, at the difference of W mostly extracted from the intrusion (Schmidt et al., 2020) and deposited in the latest veins. Concentrations of W calculated for the magmatic fluid (20-120 ppm, see above) are within the range of wolframite solubility for appropriate temperature, pressure and fluid chemistry (Wood and Samson, 2000). In Type III veins, wolframite Mn-rich chemistry reflects a high Mn concentration in the fluid consistent with Mn fluid/melt partitioning (Table A.12). However, Fe is not expected to fractionate significantly from Mn during fluid exsolution (Zajacz et al., 2008) and, so, the high fluid Mn/Fe is mainly the result of magmatic fractionation (Fig. 6). Mn-rich wolframite chemistries indicate W deposition from magmatic fluids (Michaud and Pichavant, 2019).

8. IMPLICATIONS FOR RARE ELEMENT FRACTIONATION, TRANSPORT AND DEPOSITION

Recently, fractionation in rare metal magmas has been discussed in a number of studies, several on pegmatites (Kontak and Kyser, 2009; Hulsbosch et al., 2014; 2016; Kaeter et al., 2018). As melts parental to PHP RMGs share many similarities with LCT pegmatite melts (granitic, peraluminous and felsic chemistries, high concentrations of fluxing components and rare metals, Černý et al., 2005; Linnen and Cuney, 2005; London, 2015; Villaros and Pichavant, 2019), fractionation in pegmatites is also applicable to, and testable against RMGs for which a more limited number of studies is available (Raimbault et al., 1995).

Internal differentiation in rare metal magmas has been attributed to several processes including crystal fractionation (e.g., Raimbault et al., 1995; Hulsbosch et al., 2014; Kaeter et al., 2018) and fluid saturation plus fractionation (Ballouard et al., 2016; Hulsbosch et al., 2016; Hulsbosch and Muchez, 2020). Melt-melt immiscibility has been widely advocated (Kontak and Kyser, 2009; Hulsbosch et al., 2014; Kaeter et al., 2018; Hulsbosch, 2019). Immiscible melts have been proposed to play an important role in the partitioning of elements and the transport of metals at the MHT (Thomas and Davidson, 2012; 2016). However, the presence of H_2O-,

fluxing element- and metal-rich immiscible melts has so far not found any experimental confirmation (e.g., London, 2015). At Argemela, the trace element zonation in muscovite have been satisfactorily modelled without considering any phase with unusual properties and, so, melt-melt immiscibility is not necessary. As melt composition exerts the prime control on whether immiscibility develops or not in silicate systems (Thompson et al., 2007), this conclusion can also be extended to other chemically similar rare metal magmas.

Our simple (constant melt Fe and Mn concentrations) saturation model for columbite-tantalite provides an illustration of magmatic Nb and Ta fractionation in a natural RMG. At Argemela, Nb/Ta fractionation is the consequence of (1) strongly contrasted muscovite/melt partition coefficients between Nb and Ta (respectively ~4 and ~0.6, Table A11; Raimbault, 1998; Stepanov et al., 2014) and of (2) higher solubilities of Mn and Ta than of Fe and Nb end-member CT in the melt (Linnen and Keppler, 1997; Linnen and Cuney, 2005; Van Lichtervelde et al., 2018). This explains the progressive evolution upon fractionation toward Mn-, Ta-rich columbite-tantalite compositions seen at Argemela and in other systems (Raimbault, 1998; Linnen and Cuney, 2005; Michaud et al., 2020). Cassiterite compositions also indicate progressive accumulation of Ta over Nb in the residual melt. Their Ta concentrations progressively increase with decreasing Nb/Ta and Ta_2O_5 concentrations up to > 9 wt% are attained in Cst_{II} (Michaud et al., 2020). Cassiterite saturates earlier than columbite-tantalite, i.e., at F ~ 0.5 and 0.2-0.3 respectively (see *7.2*), thus withdrawing some Nb and Ta from the melt (Table A11). This delays CT saturation and illustrates the complex interdependence between the crystallization of these two accessory phases.

The decoupling between the concentration, transport and deposition of wolframite and cassiterite as seen at Argemela is also observed in other RMGs as, for example, at Beauvoir. Indeed, cassiterite, columbite-tantalite and scarce Li-phosphates crystallize as disseminated mineralization within the Beauvoir RMG while Mn and W are deposited as scarce hübnerite in the La Bosse stockwork (Aïssa et al., 1987; Monnier et al., 2019). However, at Beauvoir and contrary to Argemela, there is a significant contribution of meteoric fluids to the hydrothermal system (Fouillac and Rossi, 1991). In peraluminous granites less evolved than RMGs, Sn, Nb, Ta and Li saturation is not generally attained during the magmatic stage because initial metal enrichments in the melt are insufficient and crystallization temperatures are inappropriate (too elevated). Consequently, during crystallization, these elements would be controlled by their partitioning between major mineral phases and melt. Micas are important repositories of rare elements in peraluminous granite magmas (Villaros and Pichavant,

2019). In less evolved magmas as in RMGs, fluid/melt partitioning controls the extraction of metals from the crystallizing magma, the subsequent behaviour of rare elements and the mineralization style. Metals of magmatic origin will be transported and eventually precipitate as the hydrothermal system evolves spatially as well as physically and chemically (e.g., Lecumberri-Sanchez et al., 2017). Elevated rare metal concentrations in the melt, MCMA and fluid partitioning are not the only factors involved in the generation of large economic Sn, W and rare element deposits. One representative example is Cínovec where intense post-magmatic subsolidus alteration is marked by the common presence of greisen and late veins (Breiter et al., 2017). Subsolidus processes can remobilize primary metal pre-concentrations originating from either MCMA or preferential partitioning in some major phases (micas). At Cínovec, greisenization led to elevated rare elements concentrations in the fluids and the formation of an economic deposit despite rare element contents in the melt being apparently low compared to Argemela. One key factor for the generation of large rare metal Variscan-type granite-related deposits is probably the building a composite igneous body made of individual intrusions with variable degrees of rare metal enrichments as a result of long-lived magmatic activity. Crystallization of each individual intrusion/stock along the MHT (following processes identified at Argemela) plus circulation of country rock fluids would drive multiple episodes of hydrothermal activity promoting the remobilization of primary rare element concentrations, their transport and concentration in the fluids and the precipitation of ore minerals.

Last, mechanisms at the MHT have practical consequences on the significance of bulk rock geochemical data. In particular, element partitioning toward the fluid can remove a significant fraction of elements from the melt. For W, calculations using partition coefficients of Tables A.11 and A.12 and an initial melt concentration of ~11 ppm (corresponding to the initial Ms_I concentration of ~22 ppm in Fig. 13b) show that the W concentration in the solid assemblage remaining after 95% crystallization and fluid exsolution (equation 16 in Spera et al., 2007) is 3 ppm, corresponding to a depletion by > 3.5 times of the initial W melt concentration. Much lower fluid partitioning-related depletions are calculated for Nb (1.1-1.2 times) but the possible presence of columbite-tantalite (and of cassiterite for Sn) raises other types of concerns. In the Argemela granite, more than 90% Nb, Ta and Sn are carried by these two accessory phases and bulk rock compositions will primarily reflect their abundance in the rock analysed ("nugget" effects) rather than true melt compositions.

ACKNOWLEDGEMENTS

The authors acknowledge Dr. A. Lima, Pr. F. Noronha, F. Pinto and R. Ribeiro for their support in the field and for discussions; P. Moutela and P. Ferraz for giving access to the Argemela quarry and the mine. Dr. I. Di Carlo (ISTO, Orléans, France) is acknowledged for assistance with the electron microprobe analyses. The authors also acknowledge Dr. T. Rigaudier and Dr. C. France-Lanord (CRPG, Nancy, France) for their help with the stable isotope study, Dr. J-L Devidal (LMV, Clermont-Ferrand, France) and Dr. P. Lach (BRGM, Orléans, France) for assistance with LA-ICP-MS analyses. This work was supported by the Labex VOLTAIRE (ANR-10-LABX-100-01), the ERAMIN project NewOres and the ANR project VARPEG (ANR-15-CE01-0001). This work has greatly benefited from the constructive remarks of three anonymous reviewers, Dr. Vasyukova and the Associate Editor Dr. Zajacz.

REFERENCES

Alderton D. H. M. and Harmon R. S. (1991) Fluid inclusion and stable isotope evidence for the origin of mineralizing fluids in south-west England. *Mineralogical Magazine* **55**, 605–611.

Aïssa M., Marignac C. and Weisbrod A. (1987) Le stockwork à ferbérite d'Echassières: evolution spatiale et temporelle; cristallochimie des ferbérites. In Cuney M. and Autran A., Géologie profonde de la France, Echassières: le forage scientifique. Une clé pour la comprehension des mécanismes magmatiques et hydrothermaux associées aux granites à métaux rares. *Géologie de la France* **2-3**, 311-333.

Audetat A., Günther D. and Heinrich C. A. (2000) Causes of large-scale metal zonation around mineralized plutons: fluid inclusion LA-ICP-MS evidence from the Mole granite, Australia. *Economic Geology* **95**, 1563-1581.

Baertschi P. and Silverman S. R. (1951) The determination of relative abundance of the oxygen isotopes in silicate rocks. *Geochimica et Cosmochimica Acta* **36**, 773-781.

Ballouard C., Poujol M., Boulvais P., Branquet Y., Tartese R. and Vigneresse J.-L. (2016) Nb-Ta fractionation in peraluminous granites: A marker of the magmatic-hydrothermal transition. *Geology* **44**, 231–234.

Belkasmi M., Cney M., Pollard P.J. and Bastoul A. (2000) Chemistry of the Ta-Nb-Sn-W oxide minerals from the Yichun rare metal granite (SE China): genetic implications and comparison with Moroccan and French Hercynian examples. *Mineralogical Magazine* **64**, 207-523.

Bettencourt J. S., Leite W. B., Goraieb C. L., Sparrenberger I., Bello R. M. S. and Payolla B. L. (2005) Sn-polymetallic greisen-type deposits associated with large-scale rapakivi granites, Brazil: fluid inclusion and stable isotope characteritics. *Lithos* **80**, 363-386.

Beus A. A. and Zalashkova N. Y. (1964) Post-magmatic high temperature metasomatic processes in granitic rocks. *International Geology Review* **6**, 668–681.

Beus A. A., Severov E. A., Sitnin A. A. and Subbotin K. D. (1962) Albitized and greisenized granites (apogranites). *Izdat Akad Nauk SSSR, Moscow*.

Bhalla P., Holtz F., Linnen R. L. and Behrens H. (2005) Solubility of cassiterite in evolved granitic melts: effect of T, fO2, and additional volatiles. *Lithos* **80**, 387-400.

Borisova A. Y., Thomas R., Salvi S., Candaudap F., Lanzanova A. and Chmeleff J. (2012) Tin and associated metal and metalloid geochemistry by femtosecond LA-ICP-QMS microanalysis of pegmatite–leucogranite melt and fluid inclusions: new evidence for melt–melt–fluid immiscibility. *Mineralogical Magazine* **76**, 91–113.

Breiter K. and Müller A. (2009) Evolution of rare-metal granitic magmas documented by quartz chemistry. *European Journal of Mineralogy* **21**, 335–346.

Breiter K., Müller A., Leichmann J. and Gabašova A. (2005) Textural and chemical evolution of a fractionated granitic system: the Podlesí stock, Czech Republic. *Lithos* **80**, 323-345.

Breiter K., Ackerman L., Svojtka M. and Müller A. (2013) Behavior of trace elements in quartz from plutons of different geochemical signature: A case study from the Bohemian Massif, Czech Republic. *Lithos* **175–176**, 54–67.

Breiter K., Ďurišová J., Hrstka T., Korbelová Z., Hložková Vaňková M., Vašinová Galiová M., Kanický V., Rambousek P., Knésl I., Dobeš P. and Dosbaba M. (2017) Assessment of magmatic vs. metasomatic processes in rare-metal granites: A case study of the Cínovec/Zinnwald Sn–W–Li deposit, Central Europe. *Lithos* **292–293**, 198–217.

Burnham C.W. (1967) Hydrothermal fluids at the magmatic stage. In Geochemistry of Hydrothermal Ore

Deposits (ed. H.L. Barnes). Holt, Rinehart, Winston, New-York, pp. 34-76.

Carignan J., Hild P., Mevelle G., Morel J. and Yeghicheyan D. (2001) Routine analyses of trace elements in geological samples using flow injection and low pressure on-line liquid chromatography coupled to ICP-MS: A study of geochemical reference materials BR, DR-N, UB-N, AN-G and GH. *Geostandards Newsletter* **25**, 187-198.

Carten R. B., Rye R. O., Landis G. P. (1988) Effects of igneous and hydrothermal processes on the composition of ore-forming fluids; stable isotope and fluid inclusion evidence, Henderson molybdenum deposit, Colorado. *Geological Society of America* **19**, A94.

Černý P., Blevin P. L., Cuney M. and London D. (2005) Granite-related ore deposits. In *Economic Geology One Hundredth Anniversary Volume* (eds J. W. Hedenquist, J. F. H. Thompson, R. J. Goldfarb and R. J. Richards). pp. 337-370.

Charoy B. and Noronha F. (1996) Multistage Growth of a Rare-Element, Volatile-Rich Microgranite at Argemela (Portugal). *Journal of Petrology* **37**, 73–94.

Charoy B., Chaudisson M. and Noronha F. (1995) Lithium zonation in white micas from the Argemela microgranite (Central Portugal): *in-situ* ion-, electron-microprobe and spectroscopic investigation. *European Journal of Mineralogy* **7**, 335-352.

Chicharro E., Boiron M.-C., López-García J. Á., Barfod D. N. and Villaseca C. (2016) Origin, ore forming fluid evolution and timing of the Logrosán Sn–(W) ore deposits (Central Iberian Zone, Spain). *Ore Geology Reviews* **72**, 896–913.

Clayton R. N. (1955) Variations in oxygen isotope abundances in rock minerals. PhD, California Institute of Technology.

Clayton R. N. and Mayeda T. K. (1963) The use of bromine pentafluoride in the extraction of oxygen from oxides and silicates for isotopic analysis. *Geochimica et Cosmochimica Acta* **27**, 43–52.

Codeço M. S., Weis P., Trumbull R. B., Glodny J., Wiedenbeck M. and Romer R. L. (2019) Boron isotope muscovite-tourmaline geothermometry indicates fluid cooling during magmatic-hydrothermal W-Sn ore formation. *Economic Geology* **114**, 153-163.

Cuney M., Marignac C. and Weisbrod A. (1992) The Beauvoir topaz-lepidolite albite granite (Massif Central, France); the disseminated magmatic Sn-Li-Ta-Nb-Be mineralization. *Economic Geology* **87**, 1766–

1794.

Duc-Tin Q., Audétat, A. and Keppler H. (2007) Solubility of tin in (Cl, F)-bearing aqueous fluids at 700°C, 140 MPa: a LA-ICP-MS study on synthetic fluid inclusions. *Geochimica Cosmochimica Acta* **71**, 3323-3335.

Fouillac A. M. and Rossi P. (1991) Near-solidus delta 18 O depletion in a Ta-Nb-bearing albite granite; the Beauvoir Granite, France. *Economic Geology* **86**, 1704–1720.

Gallego Garrido M. (1992) Las mineralizaciones de litio asociadas a magmatismo acido en Extremadura y su encadre en la zona Centro-Iberica. PhD thesis, Universidad Complutense de Madrid, 342 p.

Greenland L. P. (1970) An equation for trace element distribution during magmatic crystallization. *American Mineralogist* **55**, 455-465.

Hanson G. N. (1978) The application of trace elements to the petrogenesis of igneous rocks of granitic compositions. *Earth Planetary Science Letters* **38**, 26-43.

Haapala I. and Lukkari S. (2005) Petrological and geochemical evolution of the Kymi stock, a topaz granite cupola within the Wiborg rapakivi batholith, Finland. *Lithos* **80**, 347-362.

Harlaux M., Mercadier J., Marignac C., Peiffert C., Cloquet C. and Cuney M. (2018) Tracing metal sources in peribatholitic hydrothermal W deposits based on the chemical composition of wolframite: The example of the Variscan French Massif Central. *Chemical Geology* **479**, 58–85.

Heinrich C. A. (1990) The chemistry of hydrothermal tin(-tungsten) ore deposition. *Economic Geology* **85**, 457–481.

Holness M. B., Clemens J. D. and Vernon R. H. (2018) How deceptive are microstructures in granitic rocks? Answers from integrated physical theory, phase equilibrium, and direct observations. *Contributions to Mineralogy and Petrology* **173**, 62.

Holten T., Jamtveit B., Meakin P., Cortini M., Blundy J. and Austrheim H. (1997) Statistical characteristics of oscillatory zoning in crystals. *American Mineralogist* **82**, 596-606.

Hu S., Sun M., Yan Z., Xu J., Cao X. and Ye Y. (1984) An important metallogenetic model for W, Sn, and rare granitophile element ore deposits related to metasomatically altered granites. *Geology of granites and their metallogenetic relations international symposium, Nanjing*, 519–537.

Hulsbosch N. (2019) Nb-Ta-Sn-W Distribution in Granite-related Ore Systems: fractionation mechanisms and

examples from the Karagwe-Ankole belt of Central Africa. In *Ore Deposits* American Geophysical Union (AGU). pp. 75–107.

Hulsbosch N., Hertogen J., Dewaele S., André L. and Muchez P. (2014). Alkali metal and rare-earth element evolution of rock-forming minerals from the Gatumba area pegmatites (Rwanda): quantitative assessment of crystal-melt fractionation in the regional zonation of pegmatite groups. *Geochimica et Cosmochimica Acta* **132**, 349–374.

Hulsbosch N., Boiron M.-C., Dewaele S. and Muchez P. (2016). Fluid fractionation of tungsten during granite-pegmatite differentiation and the metal source of peribatholitic W quartz veins: evidence from the Karagwe-Ankole Belt (Rwanda). *Geochimica et Cosmochimica Acta* **175**, 299–318.

Hulsbosch N. and Muchez P. (2020). Tracing fluid saturation during pegmatite differentiation by studying the fluid inclusion evolution and multiphase cassiterite mineralisation of the Gatumba pegmatite dyke system (NW Rwanda). *Lithos* **354-355**, 105285.

Inverno C. (1998) Comments on the new findingd on the geology, geochemistry and mineralization of Argemela, Central Portugal. *Commission Insituto Geológico e Mineiro* **85**, 73-79.

Iveson A. A., Webster J. D., Rowe M. C. and Neill O. K. (2019) Fluid-melt trace-element partitioning behaviour between evolved melts and aqueous fluids: Experimental constraints on the magmatic-hydrothermal transport of metals. *Chemical Geology* **516**, 18-41.

Jahns R. H. and Burnham C. W. (1969) Experimental studies of pegmatite genesis; l, A model for the derivation and crystallization of granitic pegmatites. *Economic Geology* **64**, 843–864.

Janousek V., Moyen J.-F., Martin H., Erban V. and Farrow C. (2016) Geochemical modelling of igneous processes – principles and recipes in R language. Springer-Verlag Berlin Heidelberg. 354 p.

Kaeter D., Barros R., Menuge J. F. and Chew D. M. (2018) The magmatic–hydrothermal transition in rare-element pegmatites from southeast Ireland: LA-ICP-MS chemical mapping of muscovite and columbite–tantalite. *Geochimica et Cosmochimica Acta* **240**, 98–130.

Kelly W. C. and Rye R. O. (1979) Geologic, fluid inclusion, and stable isotope studies of the tin-tungsten deposits of Panasqueira, Portugal. *Economic Geology* **74**, 1721–1822.

Kinnaird J., Bowden P., Ixer R. A. and Odling N. W. A. (1985) Mineralogy, geochemistry and mineralization of the Ririwai complex, northern Nigeria. *Journal of African Earth Sciences* **3**, 185-222.

Kontak D. J. (2006) Nature and origin of LCT-suite pegmatite with late-stage sodium enrichment, Brazil Lake, Yarmouth County, Nova Scotia. *The Canadian Mineralogist* **44**, 563-598.

Kontak D. J. (1990) The East Kemptville topaz-muscovite leucogranite, Nova Scotia; I. Geological setting and whole-rock geochemistry. *The Canadian Mineralogist* **28**, 4:787-825.

Kontak D. J. and Kyser T. C. (2009) Nature and origin of an LCT-suite pegmatite with late-stage sodium enrichment, Brazil Lake, Yarmouth County, Nova Scotia. II. Implications of stable isotopes ($\delta^{18}O$, δD) for magma source, internal crystallization and nature of sodium metasomatism. *The Canadian Mineralogist* **47**, 745-764.

Korges M., Weis P., Lüders V. and Laurent O. (2018) Depressurization and boiling of a single magmatic fluid as a mechanism for tin-tungsten deposit formation. *Geology* **46**, 75–78.

Kovalenko V. I. (1976) Ongonites (topaz-bearing quartz keratophyre)-subvolcanic analogue of rare-metal Li-F granites. *Trans. Jt. Sov. -Mong. Sci. Res. Geol. Exped.* **15**, 128.

Lecumberri-Sanchez P., Viera R., Heinrich C. A., Pinto F. and Wälle M. (2017) Fluid-rock interaction is decisive for the formation of tungsten deposits. *Geology* **45**, 579-582.

Le Fort P., Cuney M., Deniel C., France-Lanord C., Sheppard S.M.F., Upreti B.N. and Vidal Ph. (1987) Crustal generation of the Himalayan leucogranites. *Tectonophysics* **134**, 39-57.

Lima L., Guedes A. and Noronha F. (2019) Tungsten mineralization associated with the Argemela microgranite (Central Portugal). *Journal of Iberian Geology* **45**, 625-640.

Linnen R. L. and Keppler H. (1997) Columbite solubility in granitic melts: consequences for the enrichment and fractionation of Nb and Ta in the Earth's crust. *Contrib. Mineral. Petrol*. **128**, 213-227.

Linnen R. L. and Cuney M. (2005) Granite-related rare-element deposits and experimental constraints on Ta-Nb-W-Sn-Zr-Hf mineralization, in Linnen R.L. and Samson I.M., eds., rare-element geochemistry and mineral deposits. In *Geological Association of Canada, GAC, Short Course* Canada.

London D. (2009) The origin of primary textures in granitic pegmatites. *The Canadian Mineralogist* **47**, 697-724.

London D. (2014) A petrologic assessment of internal zonation in granitic pegmatites. *Lithos* **184-187**, 74-104.

London D. (2015) Reply to Thomas and Davidson on « A petrologic assessment of internal zonation in granitic pegmatites ». *Lithos* **212-215**, 469-484.

London D., Černý P., Loomis J. and Pan J. J. (1990) Phosphorus in alkali feldspars of rare-element granitic pegmatites. *The Canadian Mineralogist* **28**, 771–786.

London D., Wolf M. B., Morgan G. B. and Garrido M. G. (1999) Experimental Silicate–Phosphate Equilibria in Peraluminous Granitic Magmas, with a Case Study of the Alburquerque Batholith at Tres Arroyos, Badajoz, Spain. *J Petrology* **40**, 215–240.

London D., Morgan G. B. VI, and Wolf M. B. (2001) Amblygonite-montebrasite solid solutions as monitors of fluorine in evolved granitic and pegmatitic melts. *American Mineralogist* **86**, 225-233.

Lukkari S. and Holtz F. (2007) Phase relations of a F-enriched peraluminous granite: an experimental study of the Kymi topaz granite stock, southern Finland. *Contributions to Mineralogy and Petrology* **153**, 273-288.

Manning D. A. C. and Hill P. I. (1990) The petrogenetic and metallogenetic significance of topaz granite from the Southwest England orefield. *Geological Society of America Special Paper* **246**, 51-69.Michaud J. A.-S. (2019) Rare metal granites: origin, emplacement and mechanisms of the magmatic-hydrothermal transition. Insights from the Argemela rare metal granite (Portugal) and an experimental study. PhD thesis, University of Orléans, 365p.

Michaud J. A.-S. and Pichavant M. (2019) The H/F ratio as an indicator of contrasted wolframite deposition mechanisms. *Ore Geology Reviews* **104**, 266–272.

Michaud J. A.-S., Gumiaux C., Pichavant M., Gloaguen E. and Marcoux E. (2020) From magmatic to hydrothermal Sn-Li-(Nb-Ta-W) mineralization: the Argemela area (central Portugal). *Ore Geology Reviews* **116**, #103215.

Monnier L., Salvi S., Melleton J., Bailly L., Béziat D., de Parseval P., Gouy S. and Lach P. (2019) Multiple generations of wolframite mineralization in the Echassieres District (Massif Central, France). *Minerals* **9**, 637.

Montel J.-M. (1993) A model for monazite/melt equilibrium and application to the generation of granitic magmas. *Chemical Geology* **110**,127–146.

Müller A. and Seltmann R. (1999) The genetic significance of snowball quartz in high fractionated tin granites of the Krušne Hory/Erzgebirge. *Mineral deposits: processes to processing* **1**, 409-412.

Müller A., Herklotz G. and Giegling H. (2018) Chemistry of quartz related to the Zinnwald/Cínovec Sn-W-Li

greisen-type deposit, Eastern Erzgebirge, Germany. *Journal of Geochemical Exploration* **190**, 357–373.

Müller A., Van den Kerkhof A. M., Behr H.-J., Kronz A. and Koch-Müller M. (2009) The evolution of late-Hercynian granites and rhyolites documented by quartz - a review. *Earth and Environmental Science Transactions of the Royal Society of Edinburg* **100**, 185-204.

Müller A., Seltmann R., Halls C., Siebel W., Dulski P., Jeffries T., Spratt J. and Kronz A. (2006) The magmatic evolution of the Land's End pluton, Cornwall, and associated pre-enrichment of metals. *Ore Geology Reviews* **28**, 329–367.

McNeil A.G., Linnen R.L., Fleming R.L. and Fayek M. (2020) An experimental approach to examine fluid-melt interaction and mineralization in rare-metal pegmatites. *American Mineralogist*, in press. DOI; https://doi.org/10.2138/am-2020-7216

O'Neil J. R. and Taylor H. P. (1969) Oxygen isotope equilibrium between muscovite and water. *Journal of Geophysical Research (1896-1977)* **74**, 6012–6022.

Pearce N. J., Perkins W., Westgate J. A., Gorton M. W., Jackson S. E., Neal C. R. and Chenery S. R. (1997) A compilation of new and published major and trace element data for NIST SRM 610 and NIST SRM 612 glass reference materials. *Geostandards and Geoanalytical Research* **21**, 115-144.

Pichavant M. (1981) An experimental study of the effect of boron on a water-saturated haplogranite at 1 kbar vapour pressure. Geological applications. *Contributions to Mineralogy and Petrology* **76**, 430-439.

Pichavant M., Boher M., Stenger J. F., Aïssa M. and Charoy B. (1987a) Relations de phases des granites de Beauvoir à 1 et 3kbar en conditions de saturation en H_2O. *Géologie de la France* **1**, 77-85.

Pichavant M., Valencia Herrera J., Boulmier S., Briqueu L., Joron J.L., Juteau M., Marin L., Michard A., Sheppard S.M.F., Treuil M. and Vernet M. (1987b) The Macusani glasses, SE Peru: evidence of chemical fractionation in peraluminous magmas. In Magmatic processes: physicochemical principles (ed. B.O. Mysen). The Geochemical Society Special Publication 1, pp. 359-373.

Pichavant M., Kontak D. J., Herrera V. and Clark A. H. (1988a) The Miocene-Pliocene Macusani Volcanics, SE Peru. I. Mineralogy and magmatic evolution of a two-mica aluminosilicate-bearing ignimbrite suite. *Contributions to Mineralogy and Petrology* **100**, 300–324.

Pichavant M., Kontak D., Briqueu L., Valencia Herrera, J. and Clark, A.H. (1988b) - The Macusani Volcanics, SE Peru: II. Geochemistry and origin of a felsic peraluminous magma. *Contributions to Mineralogy*

and Petrology **100**, 325-338.

Pichavant M., Villaros A., Deveaud S., Scaillet B. and Lahlafi M. (2016) The influence of redox state on mica crystallization in leucogranite and pegmatitic liquids. *The Canadian Mineralogist* **54**, 559-581.

Pokrovski G. S. and Schott J. (1998) Thermodynamic properties of aqueous Ge(IV) hydroxide complexes from 25 to 350°C: implications for the behavior of germanium and the Ge/Si ratio in hydrothermal fluids. *Geochimica et Cosmochimica Acta* **62**, 1631–1642.

Pollard P. J., Pichavant M. and Charoy B. (1987) Contrasting evolution of fluorine- and boron-rich tin systems. *Mineralium Deposita* **22**, 315–321.

Polya D. A., Foxford K. A., Stuart F., Boyce A. and Fallick A. E. (2000) Evolution and paragenetic context of low δD hydrothermal fluids from the Panasqueira W-Sn deposit, Portugal: new evidence from microthermometric, stable isotope, noble gas and halogen analyses of primary fluid inclusions. *Geochimica et Cosmochimica Acta* **64**, 3357–3371.

Raimbault L. (1998) Composition of complex lepidolite-type granitic pegmatites and of constituent columbite-tantalite, Chedeville, Massif Central, France. *The Canadian Mineralogist* **36**, 563-583.

Raimbault L. and Burnol L. (1998) The Richemont rhyolite dyke, Massif Central, France; a subvolcanic equivalent of rare-metal granites. *The Canadian Mineralogist* **36**, 265–282.

Raimbault L., Cuney M., Azencott C., Duthou J.-L. and Joron J. L. (1995) Geochemical evidence for a multistage magmatic genesis of Ta-Sn-Li mineralization in the granite at Beauvoir, French Massif Central. *Economic Geology* **90**, 548–576.

Rye R. O., Lufkin J. L. and Wasserman M. D. (1990) Genesis of the rhyolite-hosted tin occurrences in the black range, New Mexico, as indicated by stable isotope studies. *Geological Society of America Special Paper* **246**, 233-250.

Scaillet B., Pichavant M. and Roux J. (1995) Experimental crystallization of leucogranite magmas. *Journal of Petrology* **36**, 663-705.

Schmidt C. (2018) Formation of hydrothermal tin deposits: Raman spectroscopic evidence for an important role of aqueous Sn(IV) species. *Geochimica et Cosmochimica Acta* **220**, 499-511.

Schmidt C., Romer R. L., Wohlgemuth-Ueberwasser C. C. and Appelt O. (2020) Partitioning of Sn and W between granitic melt and aqueous fluid. *Ore Geology Reviews* **117**, #103263.

Schwartz M. O. (1992) Geochemical criteria for distinguishing magmatic and metasomatic albite-enrichment in granitoids - examples from the Ta-Li granite Yichun (China) and the Sn-W deposit Tikus (Indonesia). *Mineralium Deposita* **27**, 101-108.

Sheppard S. M. F. (1977) The Cornubian batholith, SW England: D/H and 18O/16O studies of kaolinite and other alteration minerals. *Journal of the Geological Society* **133**, 573–591.

Sheppard S. M. F. (1986) Characterization and isotopic variations in natural waters. *Reviews in Mineralogy and Geochemistry* **16**, 165-184.

Shieh Y.-N. and Zhang G.-X (1991) Stable istope studies of quartz-vein type tungsten deposits in Dajishan Mine, Jiangxi Province, Southeast China. In *Stable Isotope Geochemistry: a tribute to Samuel Epstein, Taylor H. P., O'Neil J. R. and Kaplan I. R. The Geological Society Special Publication 3.*

Simpson D. R. (1977) Aluminum phosphate variants of feldspar. *American Mineralogist* **62**, 351–355.

Sirbescu M.-L. C., Krukowski E. G., Schmidt C., Thomas R., Samson I. M. and Bodnar R. J. (2013) Analysis of boron in fluid inclusions by microthermometry, laser ablation ICP-MS and Raman spectroscopy: application to the Cryo-Genie Pegmatite, San Diego County, California, USA. *Chemical Geology* **342**, 138–150.

Smith M., Banks D. A., Yardley B. W. D. and Boyce A. (1996) Fluid inclusion and stable isotope constraints on the genesis of the Cligga Head Sn-W deposit, S.W. England. *European Journal of Mineralogy* **8**, 961–974.

Sowerby J.R. and Keppler H. (2002) The effect of fluorine, boron and excess sodium on the critical curve in the albite–H_2O system. *Contributions to Mineralogy and Petrology* **143**, 32–37.

Spera F. J., Bohrson W. A., Till C. B. and Ghiorso M. S. (2007) Partitioning of trace elements among coexisting crystals, melt and supercritical fluid during isobaric crystallization and melting. *American Mineralogist* **92**, 1881-1898.

Štemprok M. (1987) Greisenization (a review). *Geol Rundsch* **76**, 169–175.

Stepanov A., Mavrogenes J. A., Meffre S. and Davidson P. (2014) The key role of mica during igneous concentration of tantalum. *Contributions to Mineralogy and Petrology* **167**, 1009.

Sunagawa I. (1999) Growth and morphology of crystals. *Forma* **14**, 147-166.

Taylor R. (2009) Ore textures: recognition and interpretation. *Springer*, 282p.

Taylor B. E. (1986) Magmatic volatiles; Isotopic variation of C, H and S. *Reviews in Mineralogy and Geochemistry* **16**, 185–225.

Taylor B. E. and Epstein S. (1962) The relationship between O18/O16 ratios in coexisting minerals of igneous metamorphic rocks. *Bulletin of the Geological Society of America* **73**, 461-480.

Thomas R. and Davidson P. (2012) Water in granite and pegmatite-forming melts. *Ore Geology Reviews* **46**, 32-46.

Thomas R. and Davidson P. (2016) Revisiting complete miscibility between silicate melts and hydrous fluids, and the extreme enrichment of some elements in the supercritical state — Consequences for the formation of pegmatites and ore deposits. *Ore Geology Reviews* **72**, 1088–1101.

Thompson A. B., Aerts M. and Hack A. C. (2007) Liquid immiscibility in silicate melts and related systems. *Reviews in Mineralogy and Geochemistry* **65**, 99-127.

Tischendorf G., Gottesmann B., Förster H.-J. and Trumbull R. B. (1997) On Li-bearing micas: estimating Li from electron microprobe analyses and an improved diagram for graphical representation. *Mineralogical Magazine* **61**, 809-834.

Uebel P.-J. (1977) Internal structure of pagmatites, its origin and nomenclature. *Neues Jarbuch für Mineralogie Abhandlungen* **131**, 83-113.

Vallance J., Cathelineau M., Marignac C., Boiron M.-C., Fourcade S., Martineau F. and Fabre C. (2001) Microfracturing and fluid mixing in granites: W–(Sn) ore deposition at Vaulry (NW French Massif Central). *Tectonophysics* **336**, 43–61.

Van Daele J., Hulsbosch N., Dewaele S., Boiron M.-C., Piessens K., Boyce A. and Muchez P. (2018) Mixing of magmatic-hydrothermal and metamorphic fluids and the origin of peribatholitic Sn vein-type deposits in Rwanda. *Ore Geology Reviews* **101**, 481–501.

Van Lichtervelde M., Holtz F. and Melcher F. (2018) The effect of disequilibrium crystallization on Nb-Ta fractionation in pegmatites: constraints from crystallization experiments on tantalite-tapiolite. *American Mineralogist* **103**, 1401-1416.

Villaros A. and Pichavant M. (2019) Mica-liquid trace elements partitioning and the granite-pegmatite connection: the St-Sylvestre complex (Western French Massif Central). *Chemical Geology* **528**, #119265.

Watson E. B. and Harrison T. M. (1983) Zircon saturation revisited: temperature and composition effects in a variety of crustal magmas types. *Earth Planetary Science Letters* **64**, 295–304.

Wood S. A. and Samson I. M. (2000) The hydrothermal geochemistry of tungsten in granitoid environments: I. Relative solubilities of ferberite and scheelite as a function of T, P, pH, and m_{NaCl}. *Economic Geology* **95**, 143–182.

Yin L., Pollard P. J., Shouxi H. and Taylor R. G. (1995) Geologic and geochemical characteristics of the Yichun Ta-Nb-Li deposit, Jiangxi Province, South China. *Economic Geology* **90**, 577–585.

Zajacz Z., Halter W. E., Pettke T. and Guillong M. (2008) Determination of fluid/melt partition coefficients by LA-ICPMS analysis of co-existing fluid and silicate melt inclusions: Controls on element partitioning. *Geochimica et Cosmochimica Acta* **72**, 2169–2197.

Zhalashkova N. Y. and Stinin A. A. (1967) Features of the distribution of rare elements in tantalum-bearing apogranites and biotite granites. *Geochemistry International* **4**, 1013-1025.

Zhang L. F., Liu J. F. and Chen Z. S. (1989) Oxygen isotope fractionation in the quartz-water-salt system. *Economic Geology* **84**, 1643-1650.

Zhu Z., Wang R., Marignac C., Cuney M., Mercadier J., Che X. and Lespinasse M.-Y. (2018) A new style of rare metal granite with Nb-rich mica: The early Cretaceous Huangshan rare metal granite suite, northeast Jiangxi Province, southeast China. *American Mineralogist* **103**, 1530-1544.

Zoheir B., Lehmann B., Emam A., Radwan A., Rongqing Z., Bain W. M., Steele-Maclnnis M. and Nolte N. (2020) Extreme fractionation and magmatic-hydrothermal transition in the formation of the Abu Dabbab rare-metal granite, Eastern Desert, Egypt. *Lithos* **352-353**, 105329.

FIGURE CAPTIONS

Fig. 1: Geological map of the Argemela intrusion and details of the different units. (a) Inset shows location in Central Portugal and relation with the Portuguese main geological domains (GTMZ: Galicia-Tras-Os-Montes Zone; CIZ: Central Iberian Zone; OMZ: Ossa-Morena Zone; SPZ: South Portuguese Zone). The granitic facies,

the border unit and the different types of intragranitic veins are distinguished by different colours. The quarry is delineated. Note the presence of a ~N170 trending shear zone in the northeastern contact of the intrusion. SGC: Schist and Greywacke complex. (b) Schematic cross-section of the intrusion rim detailing the different units; note the complexity of the border unit.a-g refer to the illustrations of the different components in Fig. 2.

Fig. 2: Texture, geometry and mineralogy of the different facies of the Argemela granite and intragranitic veins. (a) Granitic facies. Notice the subvolcanic texture with snowball quartz (Qtz_I) and micas ($Ms_{I-II-III}$) embedded in a white fined-grained matrix; (b) fine-grained aplite (left) and coarse pegmatitic facies (right) with large K-feldspars (Kfs) and micas ($Ms_{I-II-III-IV}$) from the border unit; (c) Micaceous facies showing textures of quartz (Qtz_I) and micas ($Ms_{I-II-III}$); (d) "dyke-like" facies crosscutting the granitic facies; (e) Type I intragranitic vein with elongated quartz (Qtz_{IV}) and K-feldspar (Kfs_{II}) crystals. The margin and core of the vein are indicated. Notice the sharp contact with the granite and the lack of mineralogical transformations in the granite at the vein margin; (f) Type III intragranitic vein with quartz (Qtz_{VI}), K-feldspar (Kfs_{III}) and wolframite (Wf). The margin and core of the vein are indicated. Notice the sharp contact with the granite; (f) Arsenopyrite (Apy) crystallizing in late fractures crosscutting intragranitic veins.

Fig. 3: Cathodoluminescence (CL) and BSE images illustrating texture and zonation of quartz, micas and cassiterite of the granitic facies and border unit. (a) CL image of a snowball Qtz_I with growth zonation and albite laths underlining its euhedral habit. Note the irregular shape of the outer rim and the decreasing size of albite from core to rim. (b) CL image of interstitial Qtz_{III} overgrowing on primary Qtz_I. (c) BSE image illustrating the complex zoning of micas in the granitic facies. Note the euhedral to subhedral habit of Ms_{I-II} and compare with the irregular interstitial habit of Ms_{III} overgrowing on Ms_{I-II}. (d) BSE image illustrating the patchy aspect of Ms_{IV} invading/dissolving former $Ms_{I-II-III}$ in the border unit. (e) BSE image of interstitial Cst_{II} surrounded by Ab_{II} of the matrix and containing inclusions of CT_{II}. (f) CL image illustrating euhedral zoned Qtz_{VI} replacing Qtz_I at a vein margin close to the northeastern contact. Solid white circles and numbers represent location and size (80μm for quartz and 30μm for micas) of LA-ICP-MS analyses. See text and Table 1 for additional explanation.

Fig. 4: Whole rock major and trace element compositions of the different facies of the Argemela granite (granitic facies, border unit, "dyke-like" facies) and of granite samples in the vicinity of veins. The 4 Type III vein margins data points include 2 low-SiO_2 analyses that correspond to samples collected near the sheared contact. Data from Charoy and Noronha (1996; Argemela) and Raimbault et al. (1995; Beauvoir) are plotted for comparison, B1, B2 and B3 representing the three Beauvoir units. In the P_2O_5-SiO_2 diagram, PHP corresponds to the Peraluminous High Phosphorous group defined by Linnen and Cuney (2005).

Fig. 5: Major element chemistry of micas in the classification and nomenclature of Tischendorf et al. (1997). (a) Composition of the different mica textural types (from Ms_I to Ms_{IV}). Note that micas from the granitic facies and the border unit are plotted with the same symbol. Data on Argemela micas from Charoy et al. (1995) are shown for comparison. (b) Enlarged view of (a) detailing the compositional variations from Ms_I to Ms_{III} in a representative single crystal (see Fig. 3c and 6).

Fig. 6: Representative example of evolution of trace element concentrations from Ms_I to Ms_{III} in the granitic facies; the same trends of evolution were seen in other crystals. Note that data for Ms_{Ia}, Ms_{IIa} and Ms_{III} are mean values of the two analyses located in Fig.3c (see Table A.4). See text.

Fig. 7: Compositions of micas from the granitic facies (Gr.) and the border unit (Border). Note similarities between $Ms_{I\text{-}II\text{-}III}$ on one hand and Ms_{IV} on the other hand. See text.

Fig. 8: Trace element concentrations in quartz from the granitic (a) and the micaceous (b) facies and from Type I intragranitic vein. Note that same trends were observed for other crystals. For the granitic (a) and micaceous (b) facies, cathodoluminescence images show internal zonation in quartz and locations of analysed spots; core-rim compositional variations are illustrated for selected elements (Li, Al, Ge, Rb, Sn, B). Note the Qtz_{Ia} and Qtz_{Ib} textures in the granitic facies and the skeletal overgrowth (Qtz_{III}) on early Qtz_I in the micaceous facies. For the Type I, compositional variations are shown from analyses performed from the vein margin to its core.

Fig. 9: (a) Li (ppm), (b) Rb (ppm) and (c) Ge (ppm) concentrations plotted as a function of Al (ppm) for the different quartz generations. The general evolution from magmatic to hydrothermal is outlined. See text for details on quartz textures.

Fig. 10: $\delta^{18}O$ of micas and quartz. Micas: open diamonds, quartz: solid diamonds. Analytical uncertainties (0.1‰) are smaller than symbols.

Fig. 11: δD of (a) micas and of (b) fluids in quartz. Error bars represent calculated standard deviations given in Table 4.

Fig. 12: Model for the magmatic, magmatic-hydrothermal and early hydrothermal evolution of the Argemela intrusion. See text for discussion of crystallization stages (section 7.1) and fractionation mechanisms (section 7.4). Abbreviations: Cst: cassiterite, CT: columbite-tantalite, Li-P: montebrasite, Wf: wolframite.

Fig. 13: Results of modelling of the Sn (top) and W (bottom) concentration in muscovite during crystallization of the Argemela magma. Compositions in muscovite core (Ms_I) represented by solid black circles (average of two data points, Table A.4) and in muscovite rim (Ms_{III}) by vertical black bars (data in Table A.4). In the top diagram, the crystal fractionation model (calculated without fluid, see Appendix and text; Hanson, 1978) is shown as black solid (fraction of melt remaining $F < 0.5$) and black dashed ($F > 0.5$) curves. The SnO_2 saturation model (see Appendix and text, Janousek et al., 2016) is shown as red dashed ($F < 0.5$) and red solid ($F > 0.5$) curves. Sn concentrations in muscovite and melt are related by the muscovite/melt Sn partition coefficient (0.4, Table A.11). As F decreases, Sn concentrations build up in muscovite since Sn is incompatible (bulk $D = 0.07$, see text) but below $F = 0.5$, concentrations in the melt (black solid curve) are lower than SnO_2 saturation (red dashed curve). Crystallization of magmatic cassiterite starts at $F = 0.5$. For $F < 0.5$, Sn concentrations in the melt and muscovite are controlled by the decrease of cassiterite solubility with decreasing temperature (red solid curve). Final ($F = 0.05$) concentrations in muscovite are within the range analysed in Ms_{III}. In the bottom diagram, the crystal fractionation model is calculated without fluid (see Appendix and text, Hanson, 1978). The three other models are fluid-present and calculated with a W fluid/melt partition coefficient of 15 (Table A.12).

Two models assume constant fluid proportions of either 5% (fluid mass fraction = 0.05, green solid curve) or 10% (fluid mass fraction = 0.1, red solid curve) fluid (Appendix and text, Hanson, 1978). The third (grey solid curve) is calculated with the crystallization-fluid exsolution model (Appendix, Spera et al., 2007; Hulsbosch et al., 2016) with an initial melt water concentration of 6 wt%. The three fluid-present models simulate the progressive W depletion observed during muscovite growth. The three final (F = 0.05) concentrations bracket the range analysed in Ms_{III}. See text for discussion.

Fig. 14: δD - $\delta^{18}O$ plot for fluids in equilibrium with quartz and micas from the Argemela intrusion (calculated at 550°C) and evolution of isotopic compositions during the magmatic-hydrothermal transition. See text for details of the calculations and discussion. The magmatic and paleometeoric water boxes are from Sheppard (1986) and Polya et al. (2000). The Cornubian magmatic water and the pegmatites and skarn boxes are from Sheppard (1977) and Alderton and Harmon (1992), respectively; see also Smith et al. (1996). The quartz (Qtz) and muscovite (Ms) boxes refer to the range of isotopic compositions for these two minerals at Panasqueira (Kelly and Rye, 1979).

Appendix. Modelling of the muscovite core-rim trace element zonation

Approach. Chemical evolutions in muscovite were modelled geochemically. Elements present in dilute concentrations such as Rb, Cs, B, Mn and W, but also Li, Sn, Nb and Ta which are essential structural constituents in montebrasite, cassiterite and columbo-tantalite, were selected. Several melt crystallization models were tested. For each element, the concentration measured in muscovite core ($C_{0\ mu}$) was assumed representative of the initial melt concentration $C_{0\ l}$, with $C_{0\ mu}$ and $C_{0\ l}$ being related by the muscovite/melt partition coefficient Kd_{mu} (= $C_{0\ mu}$ / $C_{0\ l}$). The models generated melt concentrations ($C_{f\ l}$) which were recast into equilibrium muscovite concentrations ($C_{f\ mu}$) and then compared with observed types of zonation and trace element concentrations.

Models. For all trace elements, bulk distribution coefficients (D = sum of mineral/melt partition coefficients weighted by the mass fraction of the respective mineral, e.g., Hanson, 1978) were calculated using the mineral mass fractions (including accessory phases, e.g. Nb and Ta in cassiterite) and mineral/melt partition coefficients detailed below. Both fractional and equilibrium crystallization models (e.g., Hanson, 1978), with either constant or variable D formulations (Greenland, 1970), were computed. Fluid-present models were also tested using fluid/melt partition coefficients. Fractional and equilibrium calculations were performed with constant fluid mass fractions of either 0.05 or 0.1. The crystallization-fluid exsolution models of Spera et al. (2007) and Hulsbosch et al. (2016) were also tested with a H_2O solubility of 6 wt% in the melt.

For Li, Sn, Nb and Ta, saturation models were constructed for the different accessory phases since mineral saturation buffers $C_{f\,l}$ during crystallization. $C_{f\,l}$ calculated with saturation models were compared with $C_{f\,l}$ from fractionation models and the minimum values were retained (e.g., Janousek et al., 2016, their fig. 13.5).

Mass fractions. They are summarized in Table A10. For quartz, albite, muscovite and montebrasite, the modal data of Charoy and Noronha (1996) were used and, for alkali feldspar, the proportion was increased from 0.1 to 5 vol%. The mass fraction of cassiterite (0.001) was calculated by mass-balancing the Argemela granite whole-rock Sn content (Table A.2) between cassiterite (considered to be pure SnO_2) and muscovite (Table A.4). The mass fraction of columbite-tantalite was calculated in the same way from the Nb and Ta contents in whole-rock and muscovite, and the average Nb_2O_5 and Ta_2O_5 concentrations in columbite-tantalite (Michaud et al., 2020). The same result (0.0001) was obtained from either Nb or Ta.

Mineral/melt partition coefficients. Partitioning data for trace elements and phases crystallizing in rare metal granite magmas are limited (see Hulsbosch et al., 2014; Kaeter et al., 2018; Villaros and Pichavant, 2019). In this work, a trace element mineral/melt database constructed from the Macusani Volcanics, a rare volcanic equivalent of rare metal granites (Pichavant et al., 1988a; b), was used. Partition coefficients were obtained from LA-ICP-MS analysis of matrix glasses and phenocryst phases coexisting in the same thin sections. The resulting mineral/melt partition coefficients are summarized in Table A.11. For cassiterite and columbite-tantalite, partition coefficients for Nb, Ta and W were estimated (Table A.11). The presence of small amounts of SnO_2 in columbite-tantalites (Michaud et al., 2020) was ignored.

Saturation models. Simple accessory mineral saturation models were constructed by assuming that solubilities only depend on temperature, thus ignoring the influence of redox state and of fluxing elements in the melt. Solubility data (cassiterite) and solubility products (columbite-tantalite, montebrasite) were regressed as a function of temperature. Muscovite crystallization was assumed to range from 650°C (muscovite core, i.e., F= 1) to 550°C (muscovite rim, i.e., F = 0) as constrained from experimental phase equilibria on the Beauvoir granites (Pichavant et al., 1987a). For cassiterite, the

solubility data of Bhalla et al. (2005) were used and, for columbite-tantalite, the solubility products of Linnen and Keppler (1997) and Van Lichtervelde et al. (2018). For montebrasite, the solubility products were constrained from both experimental (London et al., 1999; London, 2001) and natural (Pichavant et al., 1987b; Gallego Garrido, 1992; Table A.2) data assuming constant aAl_2O_3. Concentrations of Fe and Mn (for calculation of Nb and Ta $C_{f\,l}$) and of P and F (for calculation of Li $C_{f\,l}$) were chosen consistent with results of the Fe and Mn modelling and calculated melt P, F concentrations.

The following mass-balance equation (Janousek et al., 2016, eq. 22.3) was used as a test of saturation models:

$$C_{0\,l} = F\,C_{f\,l} + (1\text{-}F)\,C_{f\,l}\,D + f_{acc}\,C_{acc} \qquad (1)$$

where f_{acc} and C_{acc} are the mass fraction and trace element concentration of the accessory phase respectively and D is the bulk distribution coefficient for all phases except the accessory mineral. C_{acc} can be expressed as a function of $C_{f\,l}$ writing: $Kd_{acc} = C_{acc} / C_{f\,l}$ where $C_{f\,l}$ is the solubility of the accessory phase in the melt (Watson and Harrison, 1983; Linnen and Keppler, 1997; Janousek et al., 2016). Accessory phase mass fractions were calculated from (1) using average Kd_{acc} values and results compared with observed abundances.

Fluid/melt partition coefficients. They are summarized in Table A.12.

Table 1

Petrographical, mineralogical and textural features of the Argemela intrusion

Stage	Occurrence	Phase	Habitus	Zoning	Textural characteristics	Ref.
Magmatic	Granitic and border unit	Qtz_I	E	x	Snowball texture (Fig. 2a; 3a); Qtz_{Ia}: core; Qtz_{Ib}: outer rim. Residual	1, 2, 3, 4
		Qtz_{II}	E		Polygonal grains sometimes forming "mosaic" pockets in the matrix	
		Ab_I	E		Inclusions in Qtz_I core (Ab_{Ia}) and rim (Ab_{Ib}; Fig. 3a)	2
		Ab_{II}	E		Main mineral in the matrix; typical albite twinning	3
		Ms_{I-II}	E	x	Ms_I: light grey (BSE imaging) euhedral core (a) evolving to a brighter rim (b); Ms_{II}: (a) darker euhedral overgrowth on Ms_I evolving to a brighter rim (b); Ms_{Ib-IIb} not always present (Fig. 3c)	3, 4
		$Li\text{-}P_I$	E-S		Twinned and associated to Cst_I	
		Cst_I	E	x	Light to dark brown, associated to $Li\text{-}P_I$	
		CT_I	S	x	Isolated black crystals	
		± Kfs_I	S		Forms tartan twinned crystals when present	
Magmatic-hydrothermal	Granitic and border unit	Qtz_{III}	I		Overgrowth on Qtz_I and invades the albitic matrix (Fig. 3b)	4, 5, 6
		Ms_{III}	I		Forms overgrowths on Ms_{I-II} and invades the matrix (Fig. 3c)	
		Cst_{II}	I	x	Found either as overgrowths on Cst_I or isolated (Fig. 3e)	
		CT_{II}	E-S	x	Inclusions in Cst_{II}	
Hydrothermal	Type I vein	Qtz_{IV}	S-A		Elongated subhedral to anhedral crystals growing perpendicularly to the vein margin (Fig. 2e)	7
		Kfs_{II}	S-A		Elongated subhedral to anhedral crystals growing perpendicularly to the vein margin (Fig. 2e)	
		$Li\text{-}P_{II}$	S-A		Discontinuous elongated crystals	
	Type II vein	Qtz_V	A		Massive crystals	
		± Li-P	S		Scarce subhedral crystals in massive quartz	
	Type III vein	Qtz_{VI}	E-S		Elongated to massive	8, 9
		Kfs_{III}	E-S		Occurring either as euhedral crystals growing from vein margins or isolated in massive quartz	
		$Li\text{-}P_{III}$	E-S			
		± Wf, CT_{III}, Cst_{III}	S-A-P		In close association either with Qtz_{VI}, Kfs_{III} and $Li\text{-}P_{III}$ or $Li\text{-}P_{III}$ only. Inclusions of CT_{III} in Wf	
	Granite at vein margins	Qtz_{VII}	E	x	Replacing Qtz_I in the granite at vein margins (Fig. 3f)	
Metasomatic	Border unit	Ms_{IV}	P		Patches invading former micas (Fig. 3d); Very bright in BSE images	
	NE sheared border	Sulphide	E		In the granite mass (pervasive) or around and inside veins (Fig. 2g)	

E: euhedral; S: subhedral; I: interstitial; A: anhedral; P: patchy. Abbreviations: Qtz: quartz, Ab: albite, Ms: muscovite, Li-P: montebrasite, Cst: cassiterite, CT: columbite-tantalite, Kfs: K-feldspar, Wf: wolframite. 1: Holten et al., 1997; 2: Müller and Seltmann, 1999; 3: Sunagawa, 1999; 4: Holness et al., 2018; 5: Raimbault et al., 1995; 6: Taylor, 2009; 7: Michaud et al., 2020; 8: Aïssa et al., 1987; 9: Monnier et al., 2019.

Table 2

Representative bulk rock analyses of the Argemela RMG

Facies	Granitic facies		"Dyke-like"	Border facies		Intragranitic veins margins				Detection limits
				Aplitic	Mica-ceous	I	II	III	III contact	
Major elements (wt %)	A2	A6	A8	A11	A9	A46	A45	A6	A49	wt%
SiO_2	68.69	69.79	71.54	64.32	65.16	69.40	70.85	69.53	66.04	0.050
TiO_2	bdl	bdl	bdl	bdl	bdl	bdl	bdl	bdl	bdl	0.100
Al_2O_3	18.27	17.57	16.44	19.86	19.24	17.72	16.85	17.93	19.98	0.060
FeO	0.36	0.27	0.15	0.15	0.57	0.33	0.21	0.25	0.37	0.030
MnO	0.023	0.020	0.022	0.016	0.046	0.05	0.02	0.02	0.03	0.010
MgO	bdl	bdl	bdl	bdl	bdl	bdl	bdl	bdl	bdl	0.040
CaO	-	-	0.03	0.45	1.71	0.32	0.05	0.11	0.33	0.100
Na_2O	4.49	5.71	2.38	8.66	4.06	6.24	6.01	6.06	4.85	0.030
K_2O	3.18	2.92	5.16	1.04	2.78	2.12	2.32	2.53	3.79	0.080
P_2O_5	1.62	1.49	1.72	2.69	2.06	1.76	1.78	1.95	1.77	0.200
F	0.31	0.29	0.26	0.27	0.54	0.43	0.28	0.29	0.33	
LOI	2.33	1.25	1.97	2.03	3.30	1.54	1.17	0.55	2.50	
O=F	0.13	0.12	0.11	0.11	0.23	0.18	0.12	0.12	0.14	
Total	98.96	99.03	99.45	99.23	98.98	99.48	99.26	98.94	99.71	
Trace elements (ppm)										ppm
B	NA	NA	87.50	NA	NA	35.80	38.30	47.90	70.70	
Li	1645	1684	1774	1688	1445	1788	2026	2026	1041	
As	28.00	0.75	0.70	21.00	0.55	1.00	bdl	0.96	90.23	0.20
Ba	11.20	6.20	15.05	33.40	19.20	8.48	6.77	bdl	14.71	2.0
Be	37.00	31.90	13.61	15.80	62.40	66.99	15.21	150.50	39.97	0.09
Bi	0.68	0.93	0.68	1.35	0.38	0.17	0.49	0.20	0.11	0.04
Cd	0.05	bdl	bdl	bdl	bdl	0.02	0.03	bdl	0.03	0.04
Ce	0.25	0.15	0.17	0.13	0.23	0.13	0.24	0.14	0.12	0.02
Co	0.12	bdl	0.10	0.08	0.10	0.13	0.12	bdl	0.15	0.075
Cr	1.70	1.70	3.61	2.10	1.80	4.42	5.20	3.51	2.69	0.5
Cs	30.10	29.40	39.22	15.00	78.30	50.03	25.35	25.41	30.63	0.02
Cu	21.60	6.30	11.77	21.70	15.40	9.26	9.83	7.19	16.74	6.0
Dy	0.07	0.01	0.02	0.08	0.06	0.06	0.01	0.01	0.04	0.005
Er	0.04	0.01	0.01	0.06	0.04	0.04	0.01	0.01	0.02	0.001
Eu	0.01	-	-	0.01	0.02	0.01	-	bdl	0.01	0.002
Ga	42.20	36.30	38.38	27.60	39.80	36.23	36.98	37.70	44.07	0.015
Gd	0.06	0.01	0.02	0.06	0.06	0.05	0.01	0.01	0.04	0.005
Ge	4.43	4.51	4.67	4.48	4.98	5.37	4.90	4.66	3.98	0.05
Hf	2.73	2.36	5.36	1.39	2.32	3.03	2.88	2.85	2.73	0.03
Ho	0.01	-	-	0.02	0.01	0.01	-	-	0.01	0.001
La	0.15	0.10	0.13	0.08	0.14	0.10	0.17	0.12	0.16	0.04
Lu	0.01	-	bdl	0.01	0.01	0.01	-	-	0.01	0.001
Nb	34.90	58.70	48.59	17.30	44.10	60.06	89.17	63.70	22.80	0.02

Nd	0.11	0.05	0.05	0.08	0.12	0.06	0.08	0.05	0.07	0.02
Ni	bdl	bdl	3.06	bdl	bdl	2.82	3.17	bdl	5.48	5.0
Pb	23.90	31.00	10	24.10	9.93	8.70	34.11	12.17	5.89	0.35
Pr	0.03	0.02	0.02	0.02	0.03	0.02	0.02	0.01	0.02	0.005
Rb	1006	949	1 442	350	1211	1068	853	915	1249	0.20
S	bdl	bdl	bdl	bdl	300	bdl	bdl	bdl	bdl	100
Sb	0.09	0.09	0.11	0.08	0.24	0.09	0.07	0.10	0.16	0.05
Sm	0.04	0.01	0.02	0.03	0.04	0.02	0.02	0.01	0.02	0.004
Sn	842	884	1 960	107	512	1682	938	1130	1116	2.0
Sr	12.60	4.60	23.54	132.00	677.00	105.11	2.67	7.55	12.23	0.70
Ta	38.90	62.90	159.62	19.60	38.80	78.51	83.98	75.81	36.16	0.002
Tb	0.01	-	-	0.01	0.01	0.01	-	-	0.01	0.001
Th	0.64	0.58	1.45	0.17	0.43	0.55	0.63	0.53	0.50	0.01
Tm	0.01	-	bdl	0.01	0.01	0.01	-	-	-	0.0005
U	7.31	8.95	9.99	8.50	8.28	10.40	6.35	10.93	5.59	0.01
W	3.89	6.26	4.16	2.91	6.16	5.96	3.12	9.96	25.91	0.70
Y	0.29	0.09	0.093	0.44	0.54	0.40	0.11	0.11	0.18	0.03
Yb	0.05	0.01	-3	0.08	0.04	0.03	0.01	0.01	0.04	0.002
Zn	79.70	51.20	29.23	24.60	114.00	58.29	53.56	50.97	57.67	5.0
Zr	14.70	13.10	15.08	9.85	16.20	15.08	15.32	15.17	15.53	0.80

bdl: below detection limit; NA : not analyzed.

Table 3

$\delta^{18}O$ data of quartz and muscovite

Facies	Quartz (‰)	Muscovite (‰)	ΔQtz-Mu
Granitic	13.7	11.7	2
Micaceous	14.5	11.7	2.8
Type I vein	14.8		
Type II vein	15.6		
Type III vein	15.5		
	15.9		
Type IIISR	16.0		

SR: Santa Rita vein

Table 4
δD (‰) data of muscovite and fluids in quartz

Muscovite	δD (‰)	Mean	σ
Granitic facies	-64.75	-64.87	0.16
	-64.98		
Micaceous facies	-67.36	-67.11	0.35
	-66.86		
Fluids in quartz	δD (‰)	Mean	σ
Granitic facies	-37.98	-35.36	7.03
	-48.49		
	-32.25		
	-26.15		
	-33.35		
	-31.69		
	-37.59		
Micaceous facies	-39.45	-41.94	3.98
	-39.85		
	-46.53		
Type I vein	-32.39	-28.50	4.42
	-27.45		
	-21.24		
	-21.51		
	-27.53		
	-33.05		
	-28.75		
	-25.09		
	-26.49		
	-34.42		
	-27.54		
	-30.06		
	-34.93		
Type II vein	-31.22	-33.46	11.91
	-23.74		
	-52.07		
	-31.07		

	-42.50		
	-20.18		
Type IIIa vein	-28.64	-28.17	2.97
	-25.00		
	-30.88		
Type IIISR	-35.34	-38.94	3.84
	-43.88		
	-39.98		
	-36.55		

SR: Santa Rita vein

Table 5

$\delta^{18}O$ and δD of fluids in equilibrium with quartz and muscovite (in ‰)

Facies		$\delta^{18}O$ mineral	$\delta^{18}O$ fluid				δD mineral	δD fluid		
Temperature (°C)			550	600	650	calc.*		550	600	650
Muscovite	Granitic	11.7	12.1	12.5	12.8	541	-64.9	-52.2	-55.6	-58.5
	Micaceous	11.7	12.1	12.5	12.8	541	-67.1	-54.4	-57.8	-60.7
Quartz	Granitic	13.7	11.5	12.1	12.5	595				
	Micaceous	14.5	12.3	12.8	13.3	526				
	Type I vein	14.8				504				
	Type II vein	15.6				454				
	Type III vein	15.5				459				
		15.9				437				
	Type IIISR	16.0				432				

SR: Santa Rita vein

*Mineral-fluid equilibration temperature calculated for $\delta^{18}O$ fluid = 12‰